Fig. 5. Transfer functions of the total baroreflex loop obtained from the 4 protocols. The gain plots, phase plots, and coherence functions are shown. The transfer gain at 0.01 Hz was smaller in the P_{70} protocol than in the P_{100} and P_{130} protocols. The transfer gain at 0.1 Hz was smaller in the P_{70} and P_{160} protocols than in the P_{100} and P_{130} protocols. The slope of decreasing gain between 0.1 and 0.5 Hz was shallower in the P_{70} than in the P_{100} protocol. Solid and dashed lines represent mean and mean $\pm$ SD values, respectively.

values in the lower frequencies were dispersed and mean phase values were deviated from $-\pi$ toward 0 rad in the P_{70} and P_{160} protocols. The coherence values were <0.5 below 0.08 Hz in the P_{70} protocol and <0.5 below 0.02 Hz in the P_{160} protocol. The coherence values appeared to be greater in the P_{100} and P_{130} protocols than in the P_{70} and P_{160} protocols.

Table 2 summarizes the statistical analysis of the obtained data. In the neural arc, $G_{0.01}$ and $G_{0.1}$ were significantly smaller in the P_{70} and P_{160} protocols than in the P_{100} and P_{130} protocols. Slope$_{0.1-0.5}$ was significantly steeper in the P_{70} and P_{160} protocols than in the P_{100} and P_{130} protocols. In the peripheral arc transfer function, $G_{0.01}$ was significantly smaller in the P_{70} than in the P_{130} protocol. $G_{0.1}$ and Slope$_{0.1-0.5}$ did not differ among the four protocols. In the total loop transfer function, $G_{0.01}$ was significantly smaller in the P_{70} protocol than in the P_{100} and P_{130} protocols. $G_{0.1}$ was significantly smaller in the P_{70} and P_{160} protocols than in the P_{100} and P_{130} protocols. Slope$_{0.1-0.5}$ was significantly less negative in the P_{70} than in the P_{100} protocol.

DISCUSSION

We have demonstrated that differences in mean input CSP significantly affect the linear transfer function of the baroreflex

neural arc estimated by a binary white noise input (Fig. 3). Changes in the neural arc transfer function observed in the animal experiment were qualitatively consistent with predictions made by the derivative-sigmoidal cascade model (Fig. 1B), reinforcing the validity of this model as a first approximation of baroreflex neural arc transfer characteristics.

Operating point dependence of baroreflex transfer characteristics. In a previous study, we (14) postulated a simple model of the baroreflex neural arc consisting of a linear derivative filter followed by a nonlinear sigmoidal component based on the input size dependence of the neural arc transfer characteristics. The same model predicted that deviation of the mean input level from the center of sigmoidal nonlinearity would decrease the gain of signal transduction mainly in the low-frequency range (Fig. 1B). The midpoint pressure for the static input-output relationship between CSP and SNA was $\sim$110–115 mmHg in anesthetized rabbits (12, 13). Hence, significant deviation of the mean input CSP from the midpoint pressure in the P_{70} and P_{160} protocols resulted in decreased transfer gain in the lower frequencies compared with the P_{100} and P_{130} protocols (Fig. 3). Generally, the interpretation of the estimated transfer function in the frequencies associated with low coherence values is difficult. This is because the low

Table 2. *Parameters of neural arc, peripheral arc, and total loop transfer functions*

	P_{70}	P_{100}	P_{130}	P_{160}
Neural arc				
$G_{0.01}$, au/mmHg	0.61±0.26†§	1.32±0.42	1.36±0.45	0.60±0.25†§
$G_{0.1}$, au/mmHg	0.86±0.31†§	2.34±0.77	2.46±0.96	1.30±0.59*‡
Slope$_{0.1-0.5}$, dB/decade	17.6±3.6†§	8.1±4.4	7.4±6.6	14.1±4.3†§
Peripheral arc				
$G_{0.01}$, mmHg/au	0.54±0.26‡	0.76±0.43	0.96±0.30	0.85±0.41
$G_{0.1}$, mmHg/au	0.22±0.11	0.19±0.08	0.22±0.09	0.16±0.10
Slope$_{0.1-0.5}$, dB/decade	−31.5±11.5	−35.6±5.2	−34.7±6.7	−33.4±7.9
Total baroreflex loop				
$G_{0.01}$	0.46±0.24*§	1.40±0.80	1.55±0.72	0.73±0.39
$G_{0.1}$	0.28±0.09*‡	0.53±0.22	0.52±0.14	0.24±0.12†§
Slope$_{0.1-0.5}$, dB/decade	−17.3±7.3*	−28.3±5.5	−26.0±11.2	−21.8±7.7

Data are means $\pm$ SD. $G_{0.01}$, $G_{0.1}$, transfer gain at 0.01 Hz and 0.1 Hz, respectively; Slope$_{0.1-0.5}$, average slope of transfer gain between 0.1 and 0.5 Hz. *$P < 0.05$, †$P < 0.01$ vs. P_{100}; ‡$P < 0.05$, §$P < 0.01$ vs. P_{130}.

coherence values indicate that the output signal contained significant noise unrelated to the input signal and/or nonlinear system response, which may hamper the accurate estimation of the transfer function. However, in our experience, the continuous phase shift over the frequency range of interest is indicative of true system dynamics in physiological systems. In addition, the decreases in the transfer gain and coherence values in the low frequencies were observed even in the noiseless simulation (Fig. 1B; $P_{C\pm40}$ and $P_{C\pm60}$). Therefore, we judged that what we observed in Fig. 3 reflected the true reality rather than the limitations in analysis. These results indicate that the derivative-sigmoidal model was able to predict operating point-dependent changes in baroreflex neural arc transfer characteristics.

In the peripheral arc transfer function, although $G_{0.01}$ was significantly smaller in the P_{70} protocol than in the P_{130} protocol, other parameters did not differ markedly among the protocols. The peripheral arc transfer functions were almost unchanged among the P_{100}, P_{130}, and P_{160} protocols. The static input-output relationship between SNA and AP is much more linear than that between CSP and SNA under normal physiological conditions (24). In addition, changes in mean SNA might have been limited, despite large changes in mean CSP, because of the significant nonlinearity in the baroreflex neural arc. Therefore, the differences in mean SNA among the P_{100}, P_{130}, and P_{160} protocols might have been sufficiently small for the peripheral arc to show a piecewise linearity in the AP response. The results are consistent with previous studies demonstrating that the peripheral arc transfer function was unchanged regardless of differences in the operating point and input power (11, 14). The difference between the P_{100} and P_{160} protocols was significant in mean AP but not in mean SNA (Table 1). We think that we could not detect the difference in mean SNA between the P_{100} and P_{160} protocols because of the large variance in SNA data.

The operating point difference affected the total loop transfer function mainly at frequencies <0.1 Hz (Fig. 5). The significant decrease in the neural arc transfer gain in the lower frequencies (Fig. 3) contributed to the decreased gain in the total loop transfer function. In contrast to the low-frequency range, the gain values above 0.3 Hz in the total loop transfer function were similar among the four protocols (Fig. 5). The fact that the transfer gain manifested different modulations between low- and high-frequency ranges implies a pitfall in the assessment of the baroreflex function with ordinary pressure perturbations as follows. In many basic and clinical settings, the baroreflex function is frequently evaluated by using a ramp pressure disturbance induced by pharmacological intervention. With such a method, the baroreflex function is evaluated only in a limited frequency bandwidth determined by the ramp speed of pressure disturbance. The baroreflex gain thus estimated may not necessarily correlate with the steady-state gain or dynamic gain in the lowest frequency, which is a most important parameter in determining the steady-state performance of the negative-feedback system.

A possible mechanism for operating point dependence in neural arc transfer characteristics. Clearly, changes in the characteristics of the linear dynamic component would also account for the operating point-dependent changes in the neural arc transfer function. However, the low coherence values associated with the decreased transfer gain in the low frequencies in the P_{70} and P_{160} protocols suggest that the nonlinear system response had increased under these conditions. If the characteristics of the dynamic component alone changed, coherence values might not have changed significantly regardless of the difference in the mean input levels. A possible mechanism for the operating point dependence of the neural arc transfer characteristics is discussed below. Figure 6 schematically illustrates signal transduction through the derivative-sigmoidal cascade model. In Fig. 6, *A–F*, the input sinusoid at CSP (*a*) is first processed by the derivative filter. The filtered output (*b*) is then fed into the sigmoidal component and converted into the output sinusoid at SNA (*c*).
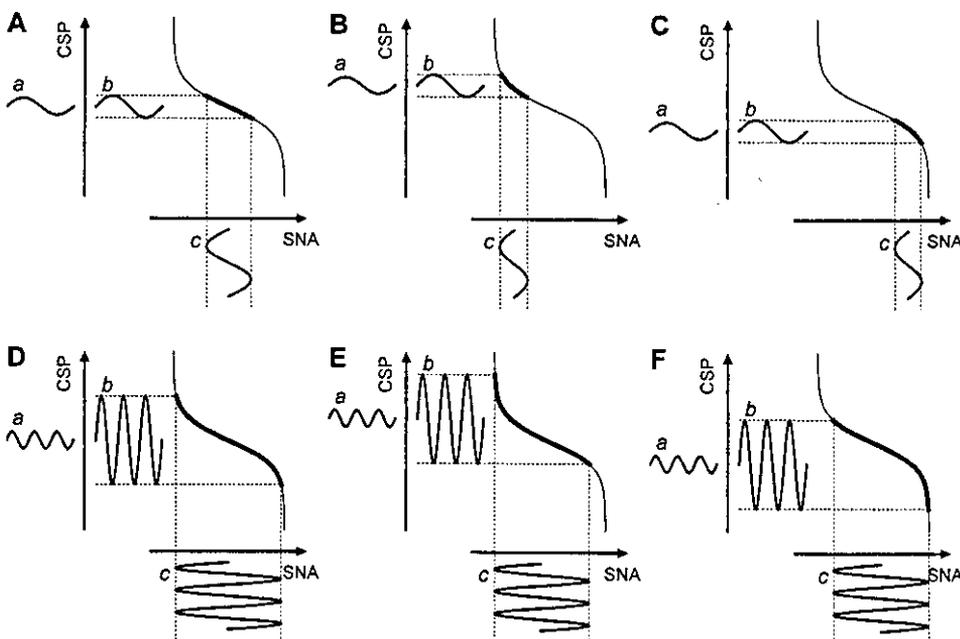

Fig. 6. Schematic diagrams of signal transduction through the derivative-sigmoidal model shown in Fig. 1A. The input sinusoid (*a*) is first processed by the derivative filter. The filtered signal (*b*) is then fed into the sigmoidal nonlinearity and converted into the output sinusoid (*c*). *A–C*: signal transduction at a low-frequency range. *D–F*: signal transduction at a high-frequency range. The operating point dependence of the signal transduction becomes unclear in the high-frequency range owing to the large amplitude of the filtered signal (*b*).

Figure 6, *A–C*, depicts signal transduction at a low-frequency range. The amplitude of the output sinusoid is maximal when the mean input level is at the center of sigmoidal nonlinearity (Fig. 6*A*). Either an increase (Fig. 6*B*) or a decrease (Fig. 6*C*) of the mean input level makes the signal transduction saturated through the sigmoidal nonlinearity, resulting in the attenuated output sinusoid. Therefore, the mean input level would critically affect the gain of the signal transduction at low frequencies.

Figure 6, *D–F*, depicts the signal transduction at a high-frequency range. The amplitude of the filtered sinusoid (*b*) becomes much greater than that at a low-frequency range, owing to the derivative filter preceding the sigmoidal nonlinearity. The large amplitude of the filtered sinusoid makes the signal transduction saturated when the mean input level is at the center of sigmoidal nonlinearity (Fig. 6*D*). On the other hand, either an increase (Fig. 6*E*) or a decrease (Fig. 6*F*) of the mean input level covers the steeper portion of sigmoidal nonlinearity compared with Fig. 6, *B* and *C*, respectively, making the saturation effect insignificant. As a result, the gain of the signal transduction becomes insensitive to the mean input level at high frequencies compared with that at low frequencies.

Limitations. First, we investigated the carotid sinus baroreflex in anesthetized rabbits. Because the anesthesia affects SNA, the results might have differed had the experiment been performed in conscious animals (27). However, the operating point dependence of the neural arc transfer characteristics may be attributable to sigmoidal nonlinearity between baroreceptor pressure input and SNA and not to the absolute value of the transfer gain. Therefore, the present results are relevant for understanding neural arc transfer characteristics under conscious conditions as well.

Second, we used a binary white noise input to estimate the baroreflex transfer characteristics. A Gaussian white noise input can yield a linear transfer function proportional to the linear part of the derivative-sigmoidal model (7). If we had used the Gaussian white noise input, therefore, the differences in mean input pressure might have demonstrated only a frequency-independent influence on the transfer gain of the baroreflex neural arc. Although the binary white noise input was useful to demonstrate the possible frequency-dependent bias in the ordinary assessment of baroreflex gain, Gaussian white noise input might be necessary for simultaneous identification of the static and dynamic characteristics of the baroreflex neural arc. Much work has been done on the identification of Wiener models (7, 17). Clearly, these identification approaches should be applied to the analysis of the transfer characteristics of the baroreflex neural arc in the future.

Finally, we sectioned vagi to remove the influences of low-pressure baroreflexes on the carotid sinus baroreflex neural arc. Accordingly, the transfer function of the total baroreflex loop shown in Fig. 5 disregarded the vagal limb of the baroreflex. Although we focused on the sympathetic limb of the carotid sinus baroreflex in the present study, further studies are clearly required to identify the neural and peripheral arcs of the vagal limb of the baroreflex.

In conclusion, the deviation of mean input pressure from the midpoint of sigmoidal nonlinearity in the CSP-SNA relationship reduced transfer gain mainly in the low-frequency range. The results obtained from the animal experiments qualitatively matched predictions based on a model consisting of a linear derivative filter, followed by a nonlinear sigmoidal component. Although simplistic, the derivative-sigmoidal cascade model functionally reproduces SNA regulation by the arterial baroreflex over a wide operating range. The present study represents an example showing the utility and strength of proper modeling in studying physiological systems.

APPENDIX

We used the MatLab Simulink toolbox (MathWorks, Natick, MA) to simulate the effects of operating point on the linear transfer function of the derivative-sigmoidal cascade model (a class of Wiener model) shown in Fig. 1*A*. We modeled the sigmoidal nonlinearity in the baroreflex neural arc by a four-parameter logistic function using *Eq. A1* (16).

$$y = \frac{p_1}{1 + \exp[p_2(x - p_3)]} + p_4 \qquad (A1)$$

where x and y are input (in mmHg) and output (in au) values of the sigmoidal nonlinearity, p_1 is the response range (in au), p_2 is the coefficient of gain, p_3 is the midpoint of input range (in mmHg), and p_4 is the minimum output value (in au). We set p_1 to be 100 au and the maximum negative gain to be -1. These settings yielded p_2 of -0.04 because the maximum negative gain equaled $p_1 p_2/4$ at $x = p_3$. We left p_3 as 0 mmHg without loss of generality, because the simulation was performed around p_3 (i.e., p_3, $p_3 \pm 20$, $p_3 \pm 40$, and $p_3 \pm 60$). We also left p_4 as 0 au, because the transfer function was calculated after subtracting the mean SNA and hence the absolute value of p_4 was meaningless. The center of the sigmoidal nonlinearity (P_C) in Fig. 1*B* corresponds to p_3.

We modeled the derivative characteristics with *Eq. A2* according to a previous study (15).

$$H(f) = \frac{1 + \dfrac{f}{f_{C1}}j}{\left(1 + \dfrac{f}{f_{C2}}j\right)^2} \exp(-2\pi f j L) \qquad (A2)$$

where f and j represent frequency (in Hz) and imaginary units, respectively, f_{C1} and f_{C2} ($f_{C1} < f_{C2}$) are the corner frequencies (in Hz) for derivative and high-cut characteristics of the neural arc, respectively, and L is the dead time (in s). We set f_{C1}, f_{C2}, and L at 0.08 Hz, 0.8 Hz, and 0.2 s, respectively. The parameter values came from the previous study (15). Note that a negative sign for negative feedback was unnecessary, as the sigmoid curve to be connected (*Eq. A1*) inverts the signal.

We simulated the SNA response to CSP perturbation according to a binary white noise sequence with a switching interval of 500 ms. The input amplitude was 20 mmHg, and the mean input level was varied from -60 to 60 mmHg around P_C with an increment of 20 mmHg. The transfer functions were calculated with the 10-Hz sampled time series data obtained from the simulations. To reduce the variance of the transfer function estimation, 100-min input-output data were provided. The deviation of mean input pressure decreased coherence values in the lower frequencies despite the noiseless nature of the simulation, indicating that the nonlinear system response reduced the coherence values.

GRANTS

REFERENCES

1. Allison JL, Sagawa K, and Kumada M. An open-loop analysis of the aortic arch barostatic reflex. *Am J Physiol* 217: 1576–1584, 1969.

2. Angell-James JE and Daly MD. Comparison of the reflex vasomotor responses to separate and combined stimulation of the carotid sinus and aortic arch baroreceptors by pulsatile and non-pulsatile pressures in the dog. *J Physiol* 209: 257–293, 1970.

3. Brigham EO. FFT transform applications. In: *The Fast Fourier Transform and Its Applications.* Englewood Cliffs, NJ: Prentice-Hall, 1988, p. 167–203.

4. Chen HI and Bishop VS. Baroreflex open-loop gain and arterial pressure compensation in hemorrhagic hypotension. *Am J Physiol Heart Circ Physiol* 245: H54–H59, 1983.

5. Glantz SA. *Primer of Biostatistics* (5th ed.). New York: McGraw-Hill, 2002.

6. Harris FJ. On the use of windows for harmonic analysis with the discrete Fourier transform. *Proc IEEE* 66: 51–83, 1978.

7. Hunter IW and Korenberg MJ. The identification of nonlinear biological systems: Wiener and Hammerstein cascade models. *Biol Cybern* 55: 135–144, 1986.

8. Ikeda Y, Kawada T, Sugimachi M, Kawaguchi O, Shishido T, Sato T, Miyano H, Matsuura W, Alexander J Jr, and Sunagawa K. Neural arc of baroreflex optimizes dynamic pressure regulation in achieving both stability and quickness. *Am J Physiol Heart Circ Physiol* 271: H882–H890, 1996.

9. Kashihara K, Kawada T, Yanagiya Y, Uemura K, Inagaki M, Takaki H, Sugimachi M, and Sunagawa K. Bezold-Jarisch reflex attenuates dynamic gain of baroreflex neural arc. *Am J Physiol Heart Circ Physiol* 285: H833–H840, 2003.

10. Kashihara K, Takahashi Y, Chatani K, Kawada T, Zheng C, Li M, Sugimachi M, and Sunagawa K. Intravenous angiotensin II does not affect dynamic baroreflex characteristics of the neural or peripheral arc. *Jpn J Physiol* 53: 135–143, 2003.

11. Kawada T, Sato T, Inagaki M, Shishido T, Tatewaki T, Yanagiya Y, Zheng C, Sugimachi M, and Sunagawa K. Closed-loop identification of carotid sinus baroreflex transfer characteristics using electrical stimulation. *Jpn J Physiol* 50: 371–380, 2000.

12. Kawada T, Shishido T, Inagaki M, Tatewaki T, Zheng C, Yanagiya Y, Sugimachi M, and Sunagawa K. Differential dynamic baroreflex regulation of cardiac and renal sympathetic nerve activities. *Am J Physiol Heart Circ Physiol* 280: H1581–H1590, 2001.

13. Kawada T, Uemura K, Kashihara K, Jin Y, Li M, Zheng C, Sugimachi M, and Sunagawa K. Uniformity in dynamic baroreflex regulation of

14. Kawada T, Yanagiya Y, Uemura K, Miyamoto T, Zheng C, Li M, Sugimachi M, and Sunagawa K. Input-size dependence of the baroreflex neural arc transfer characteristics. *Am J Physiol Heart Circ Physiol* 284: H404–H415, 2003.

15. Kawada T, Zheng C, Yanagiya Y, Uemura K, Miyamoto T, Inagaki M, Shishido T, Sugimachi M, and Sunagawa K. High-cut characteristics of the baroreflex neural arc preserve baroreflex gain against pulsatile pressure. *Am J Physiol Heart Circ Physiol* 282: H1149–H1156, 2002.

16. Kent BB, Drane JW, Blumenstein B, and Manning JW. A mathematical model to assess changes in the baroreceptor reflex. *Cardiology* 57: 295–310, 1972.

17. Korenberg MJ and Hunter IW. Two methods for identifying Wiener cascades having noninvertible static nonlinearities. *Ann Biomed Eng* 27: 793–804, 1999.

18. Marmarelis PZ and Marmarelis VZ. *Analysis of Physiological Systems. The White Noise Method in System Identification.* New York: Plenum, 1978, p. 131–221.

19. Miyano H, Kawada T, Shishido T, Sato T, Sugimachi M, Alexander J Jr, and Sunagawa K. Inhibition of NO synthesis minimally affects the dynamic baroreflex regulation of sympathetic nerve activity. *Am J Physiol Heart Circ Physiol* 272: H2446–H2452, 1997.

20. Miyano H, Kawada T, Sugimachi M, Shishido T, Sato T, Alexander J Jr, and Sunagawa K. Inhibition of NO synthesis does not potentiate dynamic cardiovascular response to sympathetic nerve activity. *Am J Physiol Heart Circ Physiol* 273: H38–H43, 1997.

21. Mohrman DE and Heller LJ. *Cardiovascular Physiology* (4th ed.). New York: McGraw-Hill, 1997, p. 151–173.

22. Sagawa K and Watanabe K. Summation of bilateral carotid sinus signals in the barostatic reflex. *Am J Physiol* 209: 1278–1286, 1965.

23. Sato T, Kawada T, Inagaki M, Shishido T, Sugimachi M, and Sunagawa K. Dynamics of sympathetic baroreflex control of arterial pressure in rats. *Am J Physiol Regul Integr Comp Physiol* 285: R262–R270, 2003.

24. Sato T, Kawada T, Inagaki M, Shishido T, Takaki H, Sugimachi M, and Sunagawa K. New analytic framework for understanding the sympathetic baroreflex control of arterial pressure. *Am J Physiol Heart Circ Physiol* 276: H2251–H2261, 1999.

25. Sato T, Kawada T, Shishido T, Sugimachi M, Alexander J Jr, and Sunagawa K. Novel therapeutic strategy against central baroreflex failure: a bionic baroreflex system. *Circulation* 100: 299–304, 1999.

26. Sato T, Kawada T, Sugimachi M, and Sunagawa K. Bionic technology revitalizes native baroreflex function in rats with baroreflex failure. *Circulation* 106: 730–734, 2002.

27. Suzuki S, Ando S, Imaizumi T, and Takeshita A. Effects of anesthesia on sympathetic nerve rhythm: power spectral analysis. *J Auton Nerv Syst* 43: 51–58, 1993.

28. Yamazaki T and Sagawa K. Summation of sinoaortic baroreflexes depends on size of input signals. *Am J Physiol Heart Circ Physiol* 257: H465–H472, 1989.

Effects of neuronal norepinephrine uptake blockade on baroreflex neural and peripheral arc transfer characteristics

Toru Kawada,[1] Tadayoshi Miyamoto,[1,2] Kazunori Uemura,[1] Koji Kashihara,[1,3] Atsunori Kamiya,[1] Masaru Sugimachi,[1] and Kenji Sunagawa[1]

[1]Department of Cardiovascular Dynamics, National Cardiovascular Center Research Institute, Osaka 565–8565; and [2]Japan Association for the Advancement of Medical Equipment, Tokyo 105–0013; and [3]Organization for Pharmaceutical Safety and Research, Tokyo 100–0013, Japan

Kawada, Toru, Tadayoshi Miyamoto, Kazunori Uemura, Koji Kashihara, Atsunori Kamiya, Masaru Sugimachi, and Kenji Sunagawa. Effects of neuronal norepinephrine uptake blockade on baroreflex neural and peripheral arc transfer characteristics. Am J Physiol Regul Integr Comp Physiol 286: R1110–R1120, 2004. First published February 12, 2004; 10.1152/ajpregu.00527.2003.—Neuronal uptake is the most important mechanism by which norepinephrine (NE) is removed from the synaptic clefts at sympathetic nerve terminals. We examined the effects of neuronal NE uptake blockade on the dynamic sympathetic regulation of the arterial baroreflex because dynamic characteristics are important for understanding the system behavior in response to exogenous disturbance. We perturbed intracarotid sinus pressure (CSP) according to a binary white noise sequence in anesthetized rabbits, while recording cardiac sympathetic nerve activity (SNA), arterial pressure (AP), and heart rate (HR). Intravenous administration of desipramine (1 mg/kg) decreased the normalized gain of the neural arc transfer function from CSP to SNA relative to untreated control (1.03 ± 0.09 vs. 0.60 ± 0.08 AU/mmHg, mean $\pm$ SE, $P < 0.01$) but did not affect that of the peripheral arc transfer function from SNA to AP (1.10 ± 0.05 vs. 1.08 ± 0.10 mmHg/AU). The normalized gain of the transfer function from SNA to HR was unaffected (1.01 ± 0.04 vs. 1.09 ± 0.12 beats·min^{-1}·AU^{-1}). Desipramine decreased the natural frequency of the transfer function from SNA to AP by $28.7 \pm 7.0\%$ (0.046 ± 0.007 vs. 0.031 ± 0.002 Hz, $P < 0.05$) and that of the transfer function from SNA to HR by $64.4 \pm 2.2\%$ (0.071 ± 0.003 vs. 0.025 ± 0.002 Hz, $P < 0.01$). In conclusion, neuronal NE uptake blockade by intravenous desipramine administration reduced the total buffering capacity of the arterial baroreflex mainly through its action on the neural arc. The differential effects of neuronal NE uptake blockade on the dynamic AP and HR responses to SNA may provide clues for understanding the complex pathophysiology of cardiovascular diseases associated with neuronal NE uptake deficiency.

systems analysis; transfer function; desipramine; sympathetic nerve activity; heart rate

NOREPINEPHRINE (NE) is released from sympathetic nerve terminals in proportion to nerve activity and removed primarily by a neuronal uptake mechanism (27). Deficiency of neuronal NE uptake results in accumulation of NE in the synaptic cleft, leading to malfunction of the dynamic sympathetic regulation of target organs. For instance, Nakahara et al. (26) demonstrated that intravenous administration of the neuronal NE uptake blocker desipramine decelerated the dynamic heart rate (HR) response to electrical stimulation of the cardiac sympathetic nerve. When the transfer function from sympathetic nerve stimulation to HR was parameterized using a second-order low-pass filter, desipramine decreased dynamic gain and lowered natural frequency of the low-pass filter. On the other hand, Bertram et al. (5) demonstrated that desipramine decreased dynamic gain but did not markedly alter natural frequency of the transfer function from lumbar sympathetic nerve stimulation to the hindlimb vascular conductance response.

Although the effects of neuronal NE uptake blockade on the dynamic sympathetic regulation have been examined using electrical stimulation of the sympathetic nerves, electrical sympathetic nerve stimulation can differ from native sympathetic discharge in its effects on target organs due to the differences in discharge pattern (9). Accordingly, the effects of neuronal NE uptake blockade on the dynamic sympathetic regulation should be reexamined using native sympathetic discharge. Further, the effects of neuronal NE uptake blockade on the overall open-loop baroreflex transfer function remain to be elucidated. Because deficiency of neuronal NE uptake is associated with a subgroup of patients with orthostatic intolerance (32, 33) or essential hypertension (30), elucidating the effects of neuronal NE uptake blockade on dynamic baroreflex function would contribute to better understanding the pathology underlying such cardiovascular diseases.

Dorward et al. (11) compared the effects of central and peripheral desipramine administrations on sympathoadrenal function and HR. In their study, intracisternal administration of desipramine attenuated changes in renal sympathetic nerve activity (SNA) in response to slow ramp changes in mean arterial pressure (AP), whereas it minimally affected the HR response. In contrast, intravenous administration of desipramine caused a baroreceptor-independent reduction in renal SNA and an augmentation of the HR response to slow ramp changes in mean AP. Although these results suggest that desipramine modulates the baroreflex function through both central and peripheral actions, how the intravenous desipramine modulates dynamic baroreflex characteristics remains to be elucidated. Bertram et al. (5) demonstrated that intravenous desipramine attenuated the dynamic AP response to the aortic depressor nerve stimulation. However, whether their results were caused by attenuation of the SNA response to depressor nerve stimulation or by attenuation of the AP response to SNA was unanswered.

We hypothesized that neuronal NE uptake blockade would blunt the dynamic sympathetic regulations of AP and HR. We

performed an open-loop experiment on the carotid sinus baroreflex in anesthetized rabbits, wherein systemic SNA was altered by way of the baroreflex (16, 17, 19–22). This experimental design enabled us to separately assess the baroreflex neural and peripheral arc transfer characteristics. The baroreflex neural arc refers to the input-output relationship between baroreceptor input pressure and SNA, whereas the baroreflex peripheral arc refers to that between SNA and AP. The following conclusions were reached from the present investigation: *1*) the neuronal NE uptake blockade by intravenous desipramine administration decreased dynamic gain of the total baroreflex mainly through attenuation of the neural arc gain, and *2*) the effects of neuronal NE uptake blockade were found to be stronger in the dynamic HR response than in the dynamic AP response to native sympathetic discharge.

MATERIALS AND METHODS

Surgical preparations. All animals used in this study were cared for in strict accordance with *Guiding Principles for the Care and Use of Animals in the Field of Physiological Sciences,* approved by the Physiological Society of Japan. Fourteen Japanese White rabbits weighing 2.7–3.6 kg were anesthetized via intravenous injection (2 ml/kg) of a mixture of urethane (250 mg/ml) and α-chloralose (40 mg/ml) and were mechanically ventilated with oxygen-enriched room air. Supplemental doses of these anesthetics were intravenously administered (0.2–0.3 ml·kg^{-1}·h^{-1}) to maintain the appropriate level of anesthesia. AP was measured using a high-fidelity pressure transducer (Millar Instruments, Houston, TX) inserted into the right femoral artery. A double-lumen catheter was introduced into the right femoral vein for drug administration. The bilateral vagi and aortic depressor nerves were sectioned at the neck to minimize any influence of cardiopulmonary and aortic arch reflexes on the baroreflex neural arc. The bilateral carotid sinuses were isolated from the systemic circulation by ligating the internal and external carotid arteries as well as other small branches originating from the carotid sinus regions (16, 17, 19–22). The isolated carotid sinuses were filled with warmed physiological saline through catheters inserted via the common carotid arteries, and the intracarotid sinus pressure (CSP) was controlled by a servocontrolled piston pump. We exposed the left cardiac sympathetic nerve through a midline thoracotomy and attached a pair of stainless steel wire electrodes (Bioflex wire AS633, Cooner Wire) to record SNA (20). The nerve fibers peripheral to the electrodes were sectioned to eliminate afferent signals from the heart. To secure the electrodes and to prevent the nerve from drying, the nerve and electrodes were soaked in silicone glue (Kwik-Sil, World Precision Instruments). The preamplified nerve signal was band-pass filtered at 150–1,000 Hz. It was then full-wave rectified and low-pass filtered with a cutoff frequency of 30 Hz to quantify the nerve activity. Pancuronium bromide (0.1 mg/kg) was given to prevent noise contamination due to muscular activity in the SNA recording. Body temperature was maintained at $\sim$38°C with a heating pad. At the end of the experiment, the experimental animal was killed by an overdose of intravenous pentobarbital sodium, and the background noise in the SNA recording was measured postmortem.

Protocols. After completing the surgical preparation, the baroreflex negative-feedback loop was functionally closed by matching CSP to AP through the servocontroller for $\sim$20 min. The servocontroller operated based on a discrete proportional-integrative-derivative control algorithm (2). The servocontrolled CSP reproduced the AP waveform up to 20 Hz, which covered approximately the fourth-order harmonics of HR frequency (4–5 Hz) in rabbits. The operating pressure was determined from mean AP at the steady state. To assess dynamic characteristics of the carotid sinus baroreflex, we randomly assigned CSP to either 20 mmHg above or below the operating pressure every 500 ms according to a binary white noise sequence (17,

19–21). The power spectral density of CSP was reasonably constant up to 1 Hz.

In *protocol 1* ($n = 7$), to examine the effects of intravenous desipramine on dynamic characteristics of the carotid sinus baroreflex, we recorded SNA, AP, and HR in response to dynamic CSP perturbation for 10 min under the control conditions (DMI$_0$) and after intravenous bolus injections of desipramine. A lower dose of desipramine (0.3 mg/kg; DMI$_{0.3}$) was examined first followed by a higher dose (1.0 mg/kg; DMI$_{1.0}$). Data recordings for DMI$_{0.3}$ and DMI$_{1.0}$ were initiated $\sim$15 min after the respective bolus injections according to a previous study (26). Effects of desipramine judged by changes in mean SNA, AP, and HR had reached steady state within this waiting period and continued for more than 10 min of the transfer function analysis.

In *protocol 2* ($n = 7$), to examine the time effects on the transfer function estimation, we repeated 10-min measurements of SNA, AP, and HR during dynamic CSP perturbation with an intervening interval of 40 min. The time interval between the first (Ctl1) and second (Ctl2) recordings corresponded to that between DMI$_0$ and DMI$_{1.0}$ in *protocol 1*.

Data analysis. We recorded CSP, SNA, AP, and HR at a sampling rate of 200 Hz using a 12-bit analog-to-digital converter. We calculated the neural arc transfer function from CSP to SNA ($H_{\text{CSP-SNA}}$), peripheral arc transfer function from SNA to AP ($H_{\text{SNA-AP}}$), and total baroreflex loop transfer function from CSP to AP ($H_{\text{CSP-AP}}$). We also estimated the transfer function from SNA to HR ($H_{\text{SNA-HR}}$). We first resampled input-output data pairs at 8 Hz and segmented them into six sets of 50% overlapping bins of 1,024 data points each (6). For each segment, a linear trend was removed and a Hanning window was applied. We then performed a fast Fourier transformation to obtain frequency spectra of the input [$X(f)$] and output [$Y(f)$]. We then ensemble averaged autospectral densities of the input [$S_{xx}(f)$] and output [$S_{yy}(f)$], and cross-spectral density between the input and output [$S_{yx}(f)$] over the six segments. Finally, we calculated the transfer function from the division of $S_{yx}(f)$ by $S_{xx}(f)$ (3, 25, 29, 34) (see Eq. A4 in APPENDIX).

To quantify the linear dependence between the input and output signals in the frequency domain, we calculated a magnitude-squared coherence function [Coh(f)] using the following equation (3, 25, 29)

$$\text{Coh}(f) = \frac{|S_{yx}(f)|^2}{S_{xx}(f)S_{yy}(f)} \qquad (1)$$

The coherence value ranges from zero to unity. A unity coherence indicates a perfect linear dependence between the input and output signals, whereas zero coherence indicates total independence between the two signals.

To facilitate the interpretation of the estimated transfer function, we calculated the system step response as follows. We obtained the impulse response from the real part of the inverse Fourier transformation of the transfer function and then calculated the step response from the time integral of the impulse response.

Statistical analysis. All data are expressed as means ± SE. In *protocol 1*, SNA was normalized in each animal so that the background noise level averaged for 1 min was zero and the SNA value averaged for the first minute in the control (DMI$_0$) condition was 100 arbitrary units (AU). We calculated mean SNA, AP, and HR by averaging respective instantaneous values for 10 min during binary white noise perturbation under DMI$_0$, DMI$_{0.3}$, and DMI$_{1.0}$ conditions.

To compare transfer functions in *protocol 1*, we determined a normalization factor so that a transfer gain value averaged below 0.024 Hz became unity in the DMI$_0$ condition. The same normalization factor was then applied to the transfer functions obtained from the DMI$_{0.3}$ and DMI$_{1.0}$ conditions. In *protocol 2*, we normalized transfer functions so that the transfer gain value averaged below 0.024 Hz became unity in the Ctl1 condition.

We parameterized $H_{CSP-SNA}$ using the following model according to previous studies (21, 22)

$$H_n(f) = -\frac{K\left(1 + \dfrac{f}{f_{c1}}j\right)}{\left(1 + \dfrac{f}{f_{c2}}j\right)^2}\exp(-2\pi f jL) \qquad (2)$$

where K, f_{c1}, f_{c2}, and L represent steady-state gain, corner frequency relating to derivative characteristics (in Hz), corner frequency relating to high-cut characteristics (in Hz), and pure delay (in s), respectively, and j represents imaginary units. The negative sign of the right-hand side of $Eq.$ 2 indicates the negative feedback attained by the baroreflex neural arc.

We parameterized H_{SNA-AP} and H_{SNA-HR} using a second-order low-pass filter with pure delay according to previous studies as follows (5, 16, 18, 22, 26)

$$H_p(f) = \frac{K}{1 + 2\zeta\dfrac{f}{f_N}j + \left(\dfrac{f}{f_N}j\right)^2}\exp(-2\pi f jL) \qquad (3)$$

where K, f_N, ζ, and L represent steady-state gain, natural frequency (in Hz), damping ratio, and pure delay (in s), respectively.

With respect to H_{CSP-AP}, although the product of $Eqs.$ 2 and 3 might yield a model transfer function for the total baroreflex loop, we did not adopt such a model because an excess number of parameters leads to large variance in the parameter estimation. Instead, we used a first-order low-pass filter with pure delay to parameterize H_{CSP-AP} as follows (16)

$$H_t(f) = -\frac{K}{1 + \dfrac{f}{f_c}j}\exp(-2\pi f jL) \qquad (4)$$

where K, f_c, and L represent steady-state gain, corner frequency (in Hz), and pure delay (in s), respectively. Some reasoning for using $Eq.$ 4 rather than the product of $Eqs.$ 2 and 3 is discussed below. First, f_{c2} in $Eq.$ 2 can be omitted, because the transfer gain of H_{CSP-AP} decreases significantly at the frequency of f_{c2} (~0.8 Hz in rabbits) and the inclusion of f_{c2} does not improve the fitting accuracy for H_{CSP-AP} much. Second, because f_{c1} in $Eq.$ 2 is close to f_N in $Eq.$ 3, zero-pole cancellation occurs in the product of $Eqs.$ 2 and 3, leaving one pole (f_c) in $Eq.$ 4.

To quantify the goodness of fit of the transfer function, we calculated the following value

$$q = 1 - \frac{\sum_{i=1}^{M}(|H(f_i) - G(f_i)|^2/i)}{\sum_{i=1}^{M}(|H(f_i)|^2/i)}, \qquad f_i = f_0 \times i \qquad (5)$$

where $H(f)$ and $G(f)$ indicate measured and model transfer functions, respectively, and f_0 indicates the fundamental frequency of Fourier transformation (0.0078 Hz). When $G(f)$ exactly matches $H(f)$, q becomes unity; q decreases from unity as the deviation of $G(f)$ from $H(f)$ increases. For $H_{CSP-SNA}$, we fit the transfer function up to 1 Hz ($M = 128$). For H_{SNA-AP}, H_{SNA-HR}, and H_{CSP-AP}, we fit the transfer function up to 0.5 Hz ($M = 64$) because the transfer function estimation became less reliable in the higher frequencies due to decreased output amplitude associated with the low-pass characteristics.

To examine the differences in the step response among DMI$_0$, DMI$_{0.3}$, and DMI$_{1.0}$ conditions in $protocol\ 1$, we calculated the steady-state step response by averaging the step response between 50 and 60 s. For the step response relating to $H_{CSP-SNA}$, the peak negative

response and the time to peak were calculated. For the step responses relating to H_{SNA-AP}, H_{SNA-HR}, and H_{CSP-AP}, the rise time was calculated as the time required for the step response to traverse the region between 10% and 80% of the steady-state response.

In $protocol\ 1$, the effects of neuronal NE uptake blockade on the respective transfer functions were examined using Dunnett's multiple comparison test following repeated-measures ANOVA (14). Mean SNA, AP, and HR were compared among DMI$_0$, DMI$_{0.3}$, and DMI$_{1.0}$ conditions using the same statistical procedure. Goodness of fit and coherence values were compared against DMI$_0$ using nonparametric multiple comparison based on ranks following Friedman test (14) as the normal distribution may not be applicable to these quantities. To examine the differences in the AP and HR responses to SNA, the parameters attained by fitting Eq. 3 to H_{SNA-AP} and H_{SNA-HR} under DMI$_0$ condition were compared by paired t-test.

In $protocol\ 2$, differences in the transfer function parameters between Ctl1 and Ctl2 conditions were examined using paired t-test. Differences in goodness of fit and coherence values between Ctl1 and Ctl2 conditions were examined using Wilcoxon signed-rank test (14) as the normal distribution may not be applicable to these quantities.

RESULTS

Figure 1 shows typical time series of CSP, SNA, AP, and HR obtained under DMI$_0$, DMI$_{0.3}$, and DMI$_{1.0}$ conditions in $protocol\ 1$. CSP was perturbed according to a binary white noise sequence. SNA, AP, and HR were changed dynamically in response to the CSP perturbation. Intravenous administration of desipramine decreased mean SNA, resulting in the decreased SNA variation in both DMI$_{0.3}$ and DMI$_{1.0}$ compared with DMI$_0$. Although mean AP decreased in DMI$_{1.0}$ compared with DMI$_0$ in Fig. 1, changes in mean AP were statistically insignificant across the animals (Table 1). Mean HR was elevated in both DMI$_{0.3}$ and DMI$_{1.0}$ compared with DMI$_0$.

Mean CSP, SNA, AP, and HR in $protocol\ 1$ are summarized in Table 1. Mean CSP was unchanged among the three conditions. Mean SNA was lower in both DMI$_{0.3}$ and DMI$_{1.0}$ than in DMI$_0$. Mean AP did not change among the three conditions. Mean HR was higher in both DMI$_{0.3}$ and DMI$_{1.0}$ than in DMI$_0$.

Figure 2A shows the group-averaged $H_{CSP-SNA}$ obtained from $protocol\ 1$. Gain plots, phase plots, and coherence functions are presented. The transfer gain increased as the frequency increased from 0.05 to 0.5 Hz in each condition, indicating derivative characteristics of the baroreflex neural arc. Intravenous desipramine administration shifted the gain plot downward in a frequency-independent manner. The phase approached $-\pi$ radians at the lowest frequency in each condition, reflecting the out-of-phase relationship between CSP and SNA at the steady state. The coherence value was below 0.5 at 0.01 Hz and increased to ~0.7 between 0.1 and 0.4 Hz in DMI$_0$. The coherence values averaged up to 1.0 Hz were 0.68 $\pm$ 0.03, 0.55 $\pm$ 0.03, and 0.52 $\pm$ 0.04 under the DMI$_0$, DMI$_{0.3}$, and DMI$_{1.0}$ conditions, respectively. The averaged coherence was significantly smaller in DMI$_{1.0}$ than in DMI$_0$ ($P < 0.05$).

Figure 2B shows the SNA step response derived from $H_{CSP-SNA}$. Desipramine significantly attenuated the negative peak response from -3.60 ± 0.40 to -2.42 ± 0.40 ($P < 0.01$) and -1.66 ± 0.33 AU ($P < 0.01$) without affecting the time to negative peak (0.71 $\pm$ 0.04, 0.77 $\pm$ 0.07, and 0.77 $\pm$ 0.07 s for DMI$_0$, DMI$_{0.3}$, and DMI$_{1.0}$, respectively). Desipramine also attenuated the steady-state response from -1.01 ± 0.23 to -0.56 ± 0.15 ($P < 0.05$) and -0.58 ± 0.09 AU ($P < 0.05$).
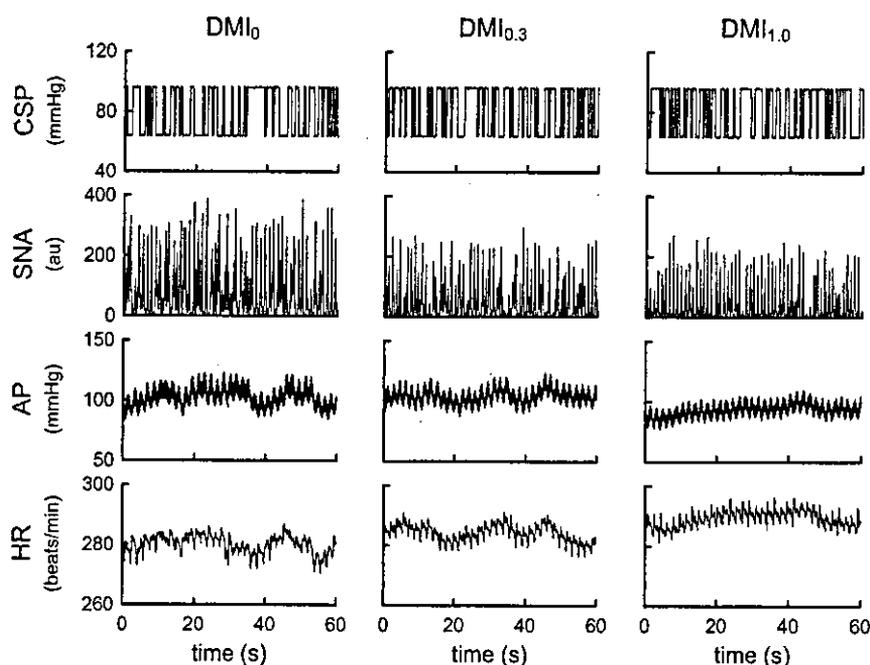
Fig. 1. Representative carotid sinus pressure (CSP), sympathetic nerve activity (SNA), arterial pressure (AP), and heart rate (HR) time series obtained under control conditions (DMI$_0$), after intravenous desipramine administration of 0.3 mg/kg (DMI$_{0.3}$), and after intravenous desipramine administration of 1.0 mg/kg (DMI$_{1.0}$) in *protocol 1*. CSP was perturbed according to a binary white noise sequence. Mean SNA decreased under DMI$_{0.3}$ and DMI$_{1.0}$ conditions compared with DMI$_0$. Changes in mean AP were not statistically significant among the protocols (Table 1). Mean HR was higher in both DMI$_{0.3}$ and DMI$_{1.0}$ than in DMI$_0$.

Figure 3A shows the group-averaged $H_{\text{SNA-AP}}$ obtained from *protocol 1*. The transfer gain decreased as the frequency increased in each condition, indicating low-pass characteristics of the baroreflex peripheral arc. The sharp peak around 0.5–0.6 Hz corresponds to the artificial ventilation frequency. The transfer gain at the lowest frequency was not altered significantly by desipramine. The phase approached zero radians at the lowest frequency, reflecting the fact that an increase in SNA led to an increase in AP at the steady state. The coherence value was ~0.6 at 0.01 Hz, increased to ~0.8 at 0.4 Hz, and decreased at higher frequencies in DMI$_0$. The coherence values averaged up to 0.5 Hz were 0.72 ± 0.07, 0.64 ± 0.08, and 0.50 ± 0.08 under the DMI$_0$, DMI$_{0.3}$, and DMI$_{1.0}$ conditions, respectively. The averaged coherence did not differ among the three conditions.

Figure 3B shows the AP step response to unit changes in SNA calculated from $H_{\text{SNA-AP}}$. Desipramine did not affect the steady-state response (1.00 ± 0.06, 1.00 ± 0.13, and 0.93 ± 0.12 mmHg under DMI$_0$, DMI$_{0.3}$, and DMI$_{1.0}$, respectively). The rise times of the step response were 12.4 ± 1.2, 14.2 ± 0.8, and 15.8 ± 0.6 s, respectively. The rise time was significantly longer in DMI$_{1.0}$ than in DMI$_0$ ($P < 0.05$).

Figure 4A shows the group-averaged $H_{\text{SNA-HR}}$ obtained from *protocol 1*. The transfer gain decreased as the frequency increased in each condition. Although desipramine did not

Table 1. *Mean levels of CSP, SNA, AP, and HR in protocol 1*

	DMI$_0$	DMI$_{0.3}$	DMI$_{1.0}$
CSP, mmHg	92±5	92±5	92±5
SNA, AU	105±1	72±4†	52±5†
AP, mmHg	89±10	92±9	83±10
HR, beats/min	277±17	289±17†	288±18*

Data are means ± SE. CSP, intracarotid sinus pressure; SNA, sympathetic nerve activity; AP, arterial pressure; HR, heart rate; DMI$_0$, control conditions; DMI$_{0.3}$ and DMI$_{1.0}$, after iv bolus injections of 0.3 and 1.0 mg/kg desipramine, respectively. *$P < 0.05$, †$P < 0.01$ vs. DMI$_0$ by Dunnett's test.

affect the transfer gain at the lowest frequency, it narrowed the flat portion in the gain plot and steepened the decreasing slope of transfer gain. The phase approached zero radians at the lowest frequency. The phase at 0.1 Hz lagged more in DMI$_{0.3}$ and DMI$_{1.0}$ than in DMI$_0$. The coherence value was ~0.6 at 0.01 Hz, increased to ~0.8 at 0.4 Hz, and then decreased at higher frequencies in DMI$_0$. The coherence values averaged up to 0.5 Hz were 0.71 ± 0.05, 0.58 ± 0.07, and 0.36 ± 0.04 under DMI$_0$, DMI$_{0.3}$, and DMI$_{1.0}$ conditions, respectively. The averaged coherence was significantly smaller in DMI$_{1.0}$ than in DMI$_0$ ($P < 0.05$).

Figure 4B shows the HR step response to unit changes in SNA calculated from $H_{\text{SNA-HR}}$. Desipramine did not affect the steady-state response (1.00 ± 0.05, 1.21 ± 0.11, and 0.98 ± 0.08 beats/min, respectively). Desipramine prolonged the rise time of the step response from 10.2 ± 1.7 to 13.2 ± 1.4 ($P < 0.05$) and 16.2 ± 0.9 s ($P < 0.01$).

Figure 5A shows the group-averaged $H_{\text{CSP-AP}}$ obtained from *protocol 1*. The transfer gain decreased as the frequency increased in each condition. Desipramine decreased the transfer gain in DMI$_{0.3}$ and DMI$_{1.0}$ compared with DMI$_0$. The phase approached $-\pi$ radians at the lowest frequency, reflecting the negative feedback attained by the total baroreflex loop. The coherence value was ~0.5 at 0.01 Hz, increased to ~0.7 in the frequency range from 0.07 to 0.3 Hz, and decreased above 0.4 Hz under the DMI$_0$ condition. The coherence values averaged up to 0.5 Hz were 0.67 ± 0.06, 0.50 ± 0.05, and 0.43 ± 0.06 under the DMI$_0$, DMI$_{0.3}$, and DMI$_{1.0}$ conditions, respectively. The averaged coherence was significantly smaller in DMI$_{1.0}$ than in DMI$_0$ ($P < 0.05$).

Figure 5B shows the AP step response corresponding to $H_{\text{CSP-AP}}$. Desipramine attenuated the steady-state response from −1.00 ± 0.06 to −0.58 ± 0.16 ($P < 0.05$) and −0.43 ± 0.10 ($P < 0.01$). Desipramine did not affect the rise time of the step response (10.8 ± 2.0, 13.5 ± 2.4, and 13.1 ± 2.7 s for DMI$_0$, DMI$_{0.3}$, and DMI$_{1.0}$, respectively).
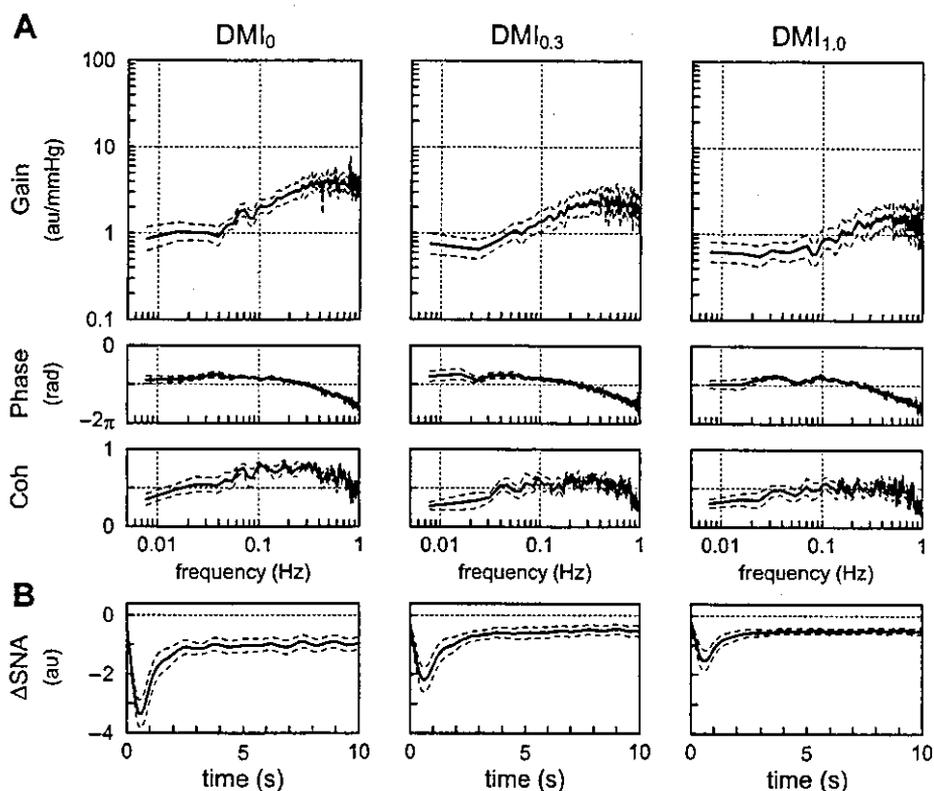
Fig. 2. *A*: neural arc transfer functions from CSP to SNA obtained from the DMI_0, $DMI_{0.3}$ and $DMI_{1.0}$ protocols in *protocol 1*. Gain plots, phase plots, and coherence functions (Coh) are shown. Desipramine administration decreased the transfer gain. *B*: step responses in SNA derived from the neural arc transfer functions. Solid and dashed lines represent mean and mean ± SE values, respectively. au, Arbitrary units. ΔSNA, change in SNA.

Table 2 summarizes the parameters of transfer functions obtained from *protocol 1*. In $H_{CSP-SNA}$, the steady-state gain was significantly smaller in $DMI_{0.3}$ and $DMI_{1.0}$ than in DMI_0. The two corner frequencies and the pure delay did not change among the three conditions. In H_{SNA-AP}, there were no significant differences in the steady-state gain among the three conditions. The natural frequency decreased to 74 ± 7% and 71 ± 7% in $DMI_{0.3}$ and $DMI_{1.0}$, respectively, compared with
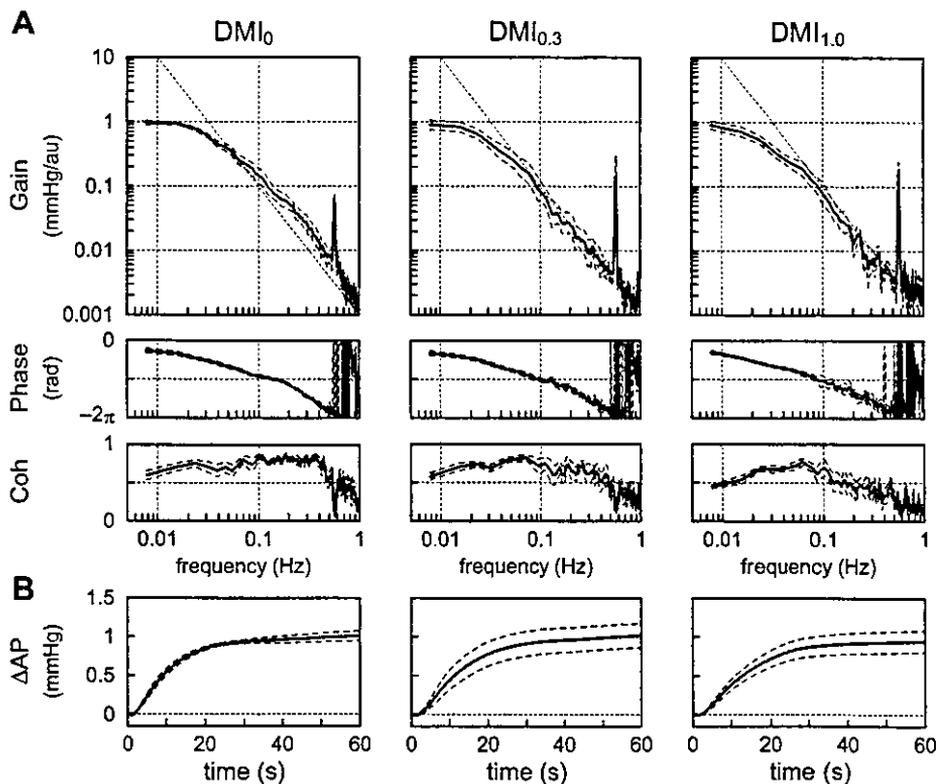

Fig. 3. *A*: peripheral arc transfer functions from SNA to AP obtained from the DMI_0, $DMI_{0.3}$ and $DMI_{1.0}$ protocols in *protocol 1*. Gain plots, phase plots, and coherence functions are shown. Desipramine administration decreased the transfer gain at higher frequencies. Dashed oblique lines in the gain plots represent a slope of −40 dB/decade. *B*: step responses in AP derived from the peripheral arc transfer functions. Solid and dashed lines represent mean and mean ± SE values, respectively. ΔAP, change in AP.
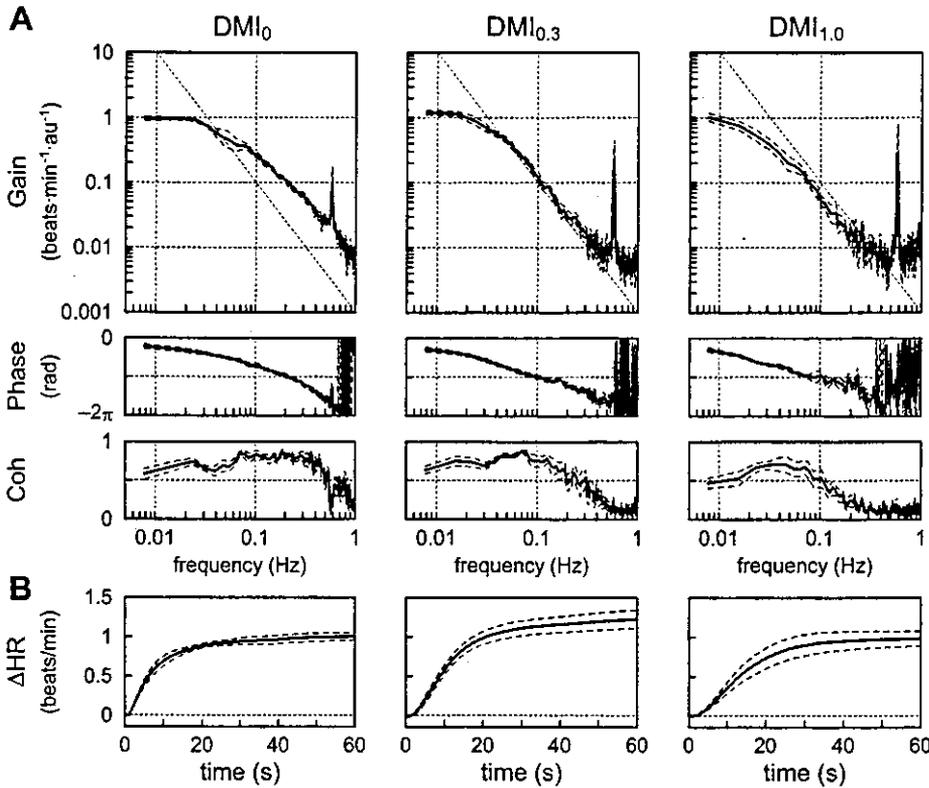
A

Fig. 4. *A*: transfer functions from SNA to HR obtained from the DMI_0, $DMI_{0.3}$ and $DMI_{1.0}$ protocols in *protocol 1*. Gain plots, phase plots, and coherence functions are shown. Desipramine administration decreased the transfer gain at high frequencies. The effects of desipramine on the gain plot were much more evident than in Fig. 3. Dashed oblique lines in the gain plots represent a slope of -40 dB/decade. *B*: step responses in HR derived from the transfer functions from SNA to HR. Desipramine slowed the HR step response. Solid and dashed lines represent mean and mean $\pm$ SE values, respectively. ΔHR, change in HR.

DMI_0. The damping ratio did not differ among the three conditions. The pure delay was significantly prolonged by desipramine in $DMI_{1.0}$. In $H_{SNA\text{-}HR}$, there were no statistical differences in the steady-state gain among the three conditions.

The natural frequency was lower in both $DMI_{0.3}$ (47 $\pm$ 4%) and $DMI_{1.0}$ (36 $\pm$ 2%) than in DMI_0. The damping ratio was significantly decreased in both $DMI_{0.3}$ and $DMI_{1.0}$. The pure delay was significantly prolonged in $DMI_{1.0}$. In $H_{CSP\text{-}AP}$, the
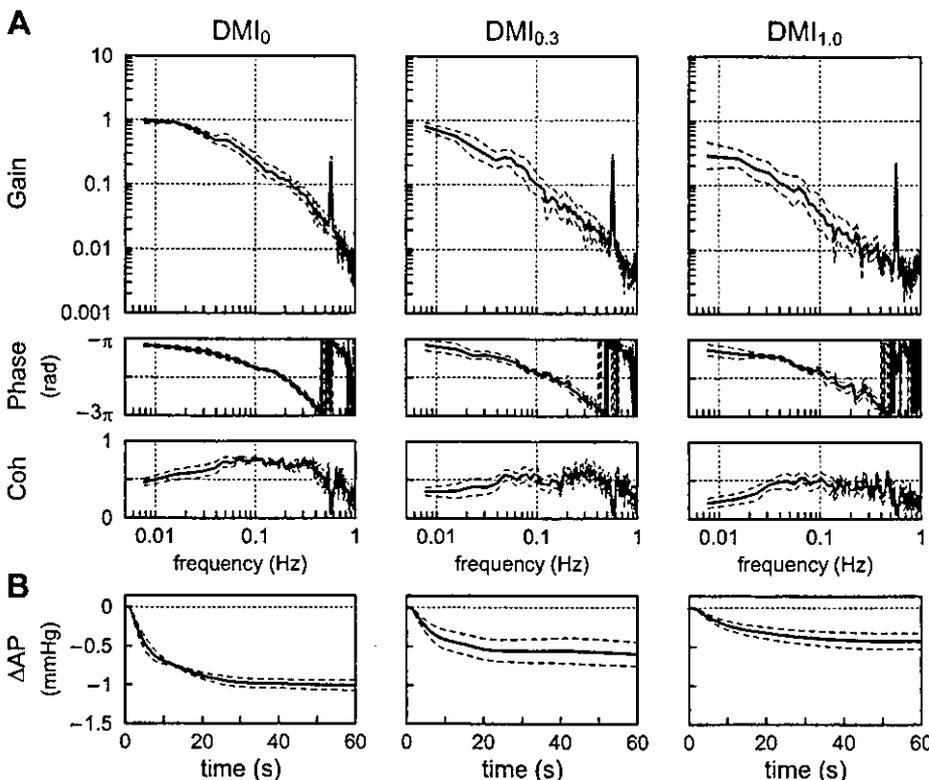
A

Fig. 5. *A*: total baroreflex loop transfer functions from CSP to AP obtained from the DMI_0, $DMI_{0.3}$ and $DMI_{1.0}$ protocols in *protocol 1*. Gain plots, phase plots, and coherence functions are shown. Desipramine administration decreased the transfer gain. *B*: step responses in AP derived from the total baroreflex loop transfer functions. Desipramine attenuated the steady-state AP response. Solid and dashed lines represent mean and mean $\pm$ SE values, respectively.

Table 2. *Effects of desipramine on transfer function parameters in protocol 1*

	DMI_0	$DMI_{0.3}$	$DMI_{1.0}$
$H_{CSP-SNA}$			
K, AU/mmHg	1.03±0.09	0.79±0.09*	0.60±0.08†
f_{c1}, Hz	0.051±0.005	0.045±0.005	0.061±0.008
f_{c2}, Hz	0.52±0.07	0.50±0.05	0.54±0.07
L, s	0.19±0.01	0.24±0.04	0.20±0.03
Goodness of fit	0.88±0.03	0.84±0.02	0.82±0.03
H_{SNA-AP}			
K, mmHg/AU	1.10±0.05	1.09±0.14	1.08±0.10
f_N, Hz	0.046±0.007	0.033±0.005*	0.031±0.002*
ζ	1.32±0.06	1.22±0.06	1.26±0.04
L, s	0.88±0.03	1.09±0.06	1.18±0.13*
Goodness of fit	0.91±0.02	0.92±0.01	0.92±0.02
H_{SNA-HR}			
K, beats·min^{-1}·AU^{-1}	1.01±0.04	1.24±0.08	1.09±0.12
f_N, Hz	0.071±0.003	0.033±0.003†	0.025±0.002†
ζ	1.60±0.08	1.15±0.08†	1.25±0.11†
L, s	0.67±0.08	0.81±0.10	1.13±0.14†
Goodness of fit	0.92±0.01	0.94±0.01	0.87±0.03
H_{CSP-AP}			
K	0.98±0.06	0.62±0.08†	0.26±0.04†
f_c, Hz	0.017±0.002	0.016±0.002	0.016±0.002
L, s	1.47±0.12	1.55±0.10	1.55±0.15
Goodness of fit	0.86±0.03	0.85±0.02	0.86±0.03

Data are means ± SE. $H_{CSP-SNA}$, neural are transfer function from CSP to SNA; H_{SNA-AP}, periperal are transfer function from SNA to AP; H_{SNA-HR}, transfer function from SNA to HR; H_{CSP-AP}, total baroreflex loop transfer function from CSP to AP; K, steady-state gain; f_{c1} and f_{c2}, corner frequencies defining the derivative and high-cut characteristics; f_N, natural frequency; f_c, corner frequency; ζ, damping ratio; L, pure delay. *$P < 0.05$, †$P < 0.01$ vs. DMI_0.

transfer gain was significantly decreased by desipramine. The corner frequency and pure delay did not differ among the three conditions. Upon comparing H_{SNA-HR} and H_{SNA-AP} under the DMI_0 condition, the natural frequency was significantly higher, the damping ratio was significantly greater, and the pure delay was significantly shorter in H_{SNA-HR} than in H_{SNA-AP}.

Figure 6 summarizes the time control for the transfer function analysis obtained from *protocol 2*. Figure 6, *A–D*, illustrates group-averaged $H_{CSP-SNA}$, H_{SNA-AP}, H_{SNA-HR}, and H_{CSP-AP}, respectively. In Fig. 6, *A–D*, the transfer functions were calculated from the first (*left*) and second (*right*) recordings with an intervening interval of 40 min. There were no significant differences in the fitted parameters between the two recordings in each of the transfer functions (Table 3).

DISCUSSION

We have examined the effects of neuronal NE uptake blockade on dynamic characteristics of the carotid sinus baroreflex. Intravenous desipramine administration decreased dynamic gain of the baroreflex neural arc, resulting in decreased dynamic gain of the total baroreflex. Natural frequency of the low-pass filter was significantly decreased by desipramine in both dynamic AP and HR responses to SNA, but to a much greater extent in the latter than the former.

Effects of desipramine on dynamic characteristics of the baroreflex neural and peripheral arcs. Intravenous desipramine administration decreased mean SNA, consistent with previous studies (5, 11, 12) (Table 1). Although reflex changes in SNA induced by changes in AP should be taken into account under baroreflex closed-loop conditions, CSP was kept con-

stant independent of AP in the present experimental settings. Thus the decrease in mean SNA was not secondary to changes in the baroreceptor pressure input. The noradrenergic neurons are located in ventral and dorsal columns in the medulla (A1 and A2 groups) (31). These neurons project to the hypothalamus and control cardiovascular and endocrine functions. In the pons the ventral column includes the A5 and A7 cell groups, which project to the spinal cord that modulates autonomic reflexes and pain sensation. The A6 cell group in the locus ceruleus has extensive projections to the cerebral cortex and cerebellum, as well as descending projections to the brain stem and spinal cord. The decreased NE clearance around these noradrenergic neurons after desipramine administration would increase the NE level in the brain stem, leading to the suppression of SNA via stimulation of the presynaptic inhibitory α_2-adrenergic receptors (8). Although desipramine could inhibit sympathetic ganglionic transmission, the preganglionic SNA also decreased during desipramine administration in a previous study (8). Therefore, the reduction of renal SNA might be attributable to the central action of desipramine.

The present results suggest that, for the first time to our best knowledge, desipramine suppressed not only mean SNA but also the transfer gain from CSP to SNA (Fig. 2, Table 2). Changes in the transfer function were not resulting from the effects of elapsed time, as the transfer function did not differ between Ctl1 and Ctl2 in *protocol 2* (Fig. 6, Table 3). The derivative characteristics of the baroreflex neural arc were preserved despite the significant loss of transfer gain under the desipramine treatment. The attenuation of SNA response to changes in CSP is in line with the human study by Tank et al. (36) wherein the neuronal NE uptake inhibition by reboxetine impaired the ability of vasomotor center to respond to sympathetic stimuli. Bertram et al. (5) demonstrated that intravenous desipramine administration almost halved dynamic gain of the transfer function from aortic depressor nerve stimulation to AP. However, whether the transfer function from aortic depressor nerve stimulation to SNA or that from SNA to AP was responsible for the reduced dynamic gain was undetermined in their study. We speculate that changes in the neural arc account for the desipramine-induced reduction of the baroreflex dynamic gain during aortic depressor nerve stimulation.

The steady-state gain of the baroreflex peripheral arc was not attenuated by desipramine (Fig. 3, Table 2), contrasting with the decreased transfer gain of the hindlimb vascular conductance response to electrical stimulation of the lumbar sympathetic chain reported by Bertram et al. (5). The preserved steady-state gain of the transfer function from SNA to HR after desipramine (Fig. 4, Table 2) was also inconsistent with our previous study (26), wherein intravenous desipramine decreased the transfer gain of the HR response to electrical stimulation of the cardiac sympathetic nerve. The apparent contradictions may be explained as follows. Intravenous desipramine decreases the transfer gain in H_{SNA-AP} or H_{SNA-HR} via the peripheral effect if mean SNA during the dynamic sympathetic perturbation is unchanged such as in the case of electrical stimulation experiments. However, mean SNA was significantly decreased by intravenous desipramine in the present experimental settings. According to previous studies, mean SNA during the dynamic sympathetic perturbation has significant influence on the transfer function from SNA to HR (4, 26): an increase in mean SNA decreases the transfer gain, and vice versa. An increase in mean SNA accumulates NE in the synaptic
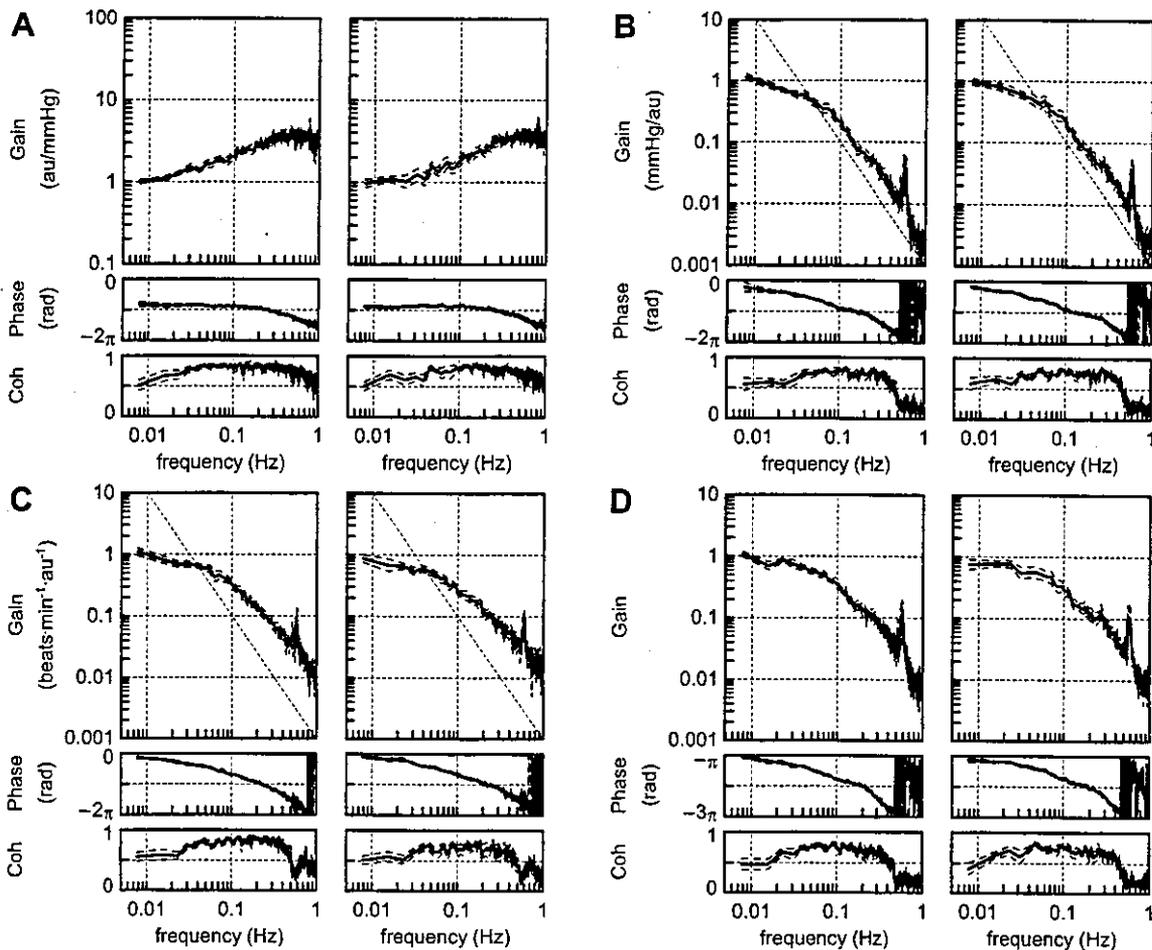
Fig. 6. Transfer functions from CSP to SNA (A), SNA to AP (B), SNA to HR (C), and CSP to AP (D) obtained from *protocol 2*. In each panel, the *left* and *right* plots represent transfer functions estimated from the first (Ctl1) and second (Ctl2) recordings with an intervening interval of 40 min, respectively. There were no significant time effects on the transfer function estimations (see Table 3). Solid and dashed lines represent mean and mean ± SE values, respectively. In B and C, dashed oblique lines in the gain plots represent a slope of −40 dB/decade.

cleft, probably reducing relative changes in the NE concentration per nerve impulse and attenuating the dynamic response of a target organ. Activation of presynaptic α_2-adrenergic receptors may also inhibit the amount of NE release per nerve impulse, reducing the transfer gain. The decrease in mean SNA via the central effect of desipramine, which itself is expected to increase the transfer gain, might have counteracted the inhibitory peripheral effect of desipramine, rendering the steady-state gain in H_{SNA-AP} or H_{SNA-HR} unchanged in the present study.

Differential effects of intravenous desipramine on the AP and HR responses. As shown in Figs. 3 and 4, low-pass characteristics of the dynamic sympathetic regulation differed between the AP and HR responses in the control (DMI₀) condition. The natural frequency was significantly higher and the damping ratio was significantly greater in H_{SNA-HR} than H_{SNA-AP}, suggesting that HR responded more quickly to SNA than AP did under control conditions. Although intravenous desipramine lowered the natural frequency of both H_{SNA-HR} and H_{SNA-AP}, the effects of desipramine were much stronger on H_{SNA-HR} than H_{SNA-AP}. Because changes in HR could affect AP and because we did not pace the heart, changes in H_{SNA-AP} might in part result from changes in H_{SNA-HR}. However, the relatively small change in the natural frequency of H_{SNA-AP}

compared with H_{SNA-HR} suggests a limited influence of the dynamic HR response on the dynamic AP response. Liu et al. (24) provided a similar result that the contribution of HR to dynamic AP regulation was negligible in anesthetized rabbits. Because cardiac output is chiefly determined by venous return under conditions of normal cardiac function and normal HR ranges, changes in the dynamic HR response alone could not significantly affect the dynamic AP regulation.

The differential effects of neuronal NE uptake blockade on the AP and HR responses have been explained by the fact that the synaptic cleft is narrower in the heart than in the vasculature (28). Because of these morphological differences, the removal of NE from the synaptic cleft is far more dependent on neuronal NE uptake in the heart than in the vascular bed (15). The effects of neuronal NE uptake blockade on the dynamic sympathetic regulation of target organs have been examined using electrical stimulation of the sympathetic nerves (5, 26) without taking into account the differences in the pattern and frequencies between electrical stimulation and native sympathetic discharge. In the present study, the differential effects of neuronal NE uptake blockade on dynamic AP and HR responses were confirmed using native sympathetic discharge.

Table 3. *Effects of elapsed time on transfer function parameters in protocol 2*

	Ctl1	Ctl2	P Value
$H_{CSP \cdot SNA}$			
K, AU/mmHg	1.05±0.04	0.94±0.09	0.17
f_{C1}, Hz	0.064±0.004	0.067±0.008	0.74
f_{C2}, Hz	0.47±0.03	0.52±0.03	0.24
L, s	0.20±0.02	0.20±0.02	0.98
Goodness of fit	0.88±0.02	0.87±0.02	NS
$H_{SNA \cdot AP}$			
K, mmHg/AU	1.10±0.03	1.09±0.11	0.83
f_N, Hz	0.053±0.005	0.056±0.006	0.45
ζ	1.32±0.11	1.34±0.16	0.94
L, s	0.84±0.09	0.82±0.08	0.76
Goodness of fit	0.88±0.05	0.88±0.06	NS
$H_{SNA \cdot HR}$			
K, beats·min^{-1}·AU^{-1}	1.03±0.06	0.96±0.13	0.77
f_N, Hz	0.10±0.008	0.094±0.006	0.49
ζ	1.59±0.12	1.53±0.13	0.65
L, s	0.75±0.05	0.68±0.05	0.21
Goodness of fit	0.91±0.03	0.87±0.04	NS
$H_{CSP \cdot AP}$			
K	1.08±0.08	1.03±0.15	0.60
f_c, Hz	0.021±0.003	0.021±0.002	0.94
L, s	1.51±0.07	1.43±0.07	0.08
Goodness of fit	0.90±0.02	0.89±0.03	NS

Data are means ± SE. Ctl1 and Ctl2 indicate repeated measurements of control conditions with an intervening interval of 40 min in *protocol 2*. *P* value was derived from paired *t*-test. The goodness of fit was tested by Wilcoxon signed-rank test. NS, not significant.

Limitations. There are several limitations to the present study. First, as anesthesia affects autonomic nervous activity (35), the results might have been different had we performed our experiments on conscious animals. However, the central and peripheral effects of desipramine observed are qualitatively consistent with those obtained from conscious rats (7). Therefore, it is possible that the anesthesia did not affect our results much.

.Second, we represented SNA responsible for the AP regulation by the left cardiac SNA, because we aimed to identify the transfer function from SNA to HR using native sympathetic discharge. However, renal SNA is more frequently investigated with respect to the AP control. As the regional differences in SNA might exist in response to changes in CSP, utilizing SNA from a different neural district might affect the estimation of the neural and peripheral arc transfer functions. However, our previous study demonstrated only a slight difference in the derivative characteristics between cardiac SNA and renal SNA in response to CSP perturbation (19). Because changes in CSP induce systemic sympathetic responses, the regional difference in SNA might not have been manifested in the present experimental protocol.

Third, we focused on the sympathetic limb of the dynamic baroreflex controls of AP and HR. We sectioned the vagi at the neck to minimize the effects of reflexes from the cardiopulmonary region on the transfer function estimation. However, the vagal efferent fibers should play a critical role in the dynamic baroreflex control of HR, because the vagal control is much faster than the sympathetic control (4, 18). Although desipramine is the least potent antimuscarinic compound among the tricyclic antidepressants (10), it could affect the vagal control of HR via the interaction between the vagal and sympathetic systems (18, 23). Further studies are required to elucidate the effects of desipramine on the dynamic vagal control of HR.

The final limitation stems from the fact that we performed the surgical preparation on the carotid sinus regions. Therefore, the carotid sinus baroreflex might be impaired to a variable extent and the estimated transfer gain values should be interpreted as relative ones. Further, this surgical preparation did not eliminate a possible feedback sympathetic control on the carotid sinus baroreflex. In an identical input pressure, an increase in the sympathetic outflow increases carotid sinus afferent nerve activity (13). Alteration of this local circuit by desipramine might have participated in the observed changes in the baroreflex dynamic characteristics. To address this question, further studies are required where carotid sinus nerve activity is measured during desipramine administration.

In conclusion, neuronal NE uptake blockade reduced the total baroreflex gain mainly though attenuation of the neural arc gain. The effects of desipramine differed between dynamic sympathetic controls of HR and AP as consistent with the results obtained by electrical stimulation of the sympathetic nerve; the HR response was more decelerated than the AP response by desipramine. In both HR and AP responses, however, the transfer gain at the lowest frequency was unaffected by desipramine, contrasting to the results obtained by electrical stimulation of the sympathetic nerve. The suppression of mean SNA via the central effects of desipramine might have prevented the complete saturation of NE kinetics at the synaptic cleft, preserving the transfer gain at a basal level in the lowest frequency. The diverse effects of neuronal NE uptake blockade observed here may underlie the complex pathophysiology in a subgroup of patients with orthostatic intolerance or essential hypertension related to neuronal NE uptake deficiency.

APPENDIX

Mathematical basis for "white-noise analysis." We assume that a system under study is regarded as time invariant within a time window of interest. We also assume that the system is regarded as linear when the input range is limited around the operating point of the system. The output of such a linear time invariant system is expressed as

$$y(t) = h(t)*x(t) + n(t) = \int_{-\infty}^{\infty} h(\tau)x(t - \tau)d\tau + n(t) \quad (A1)$$

where $x(t)$ and $y(t)$ are the input and output signals of the system, respectively; $h(t)$ is the system impulse response; $*$ denotes the convolution operator; τ is a time variable; and $n(t)$ represents noise in terms of a linear systems analysis. The noise may include physiological signal unrelated to the input, nonlinear system response, and physical noise in the signal measurement.

The frequency-domain representation of *Eq. A1* is

$$Y(f) = H(f)X(f) + N(f) \quad (A2)$$

where $X(f)$, $Y(f)$, $N(f)$, and $H(f)$ are Fourier transforms of $x(t)$, $y(t)$, $n(t)$, and $h(t)$, respectively. $H(f)$ represents the system transfer function. The convolution operator in the time domain is changed to the algebraic multiplication in the frequency domain. Multiplying the complex conjugate of $X(f)$ [$X(f)^*$] with both sides of Eq. A2 and ensemble averaging them over multiple segments yields

$$E[Y(f)X(f)^*] = H(f)E[X(f)X(f)^*] + E[N(f)X(f)^*] \quad (A3)$$

where $E[\cdot]$ indicates the ensemble average operation. Note that $H(f)$ is time invariant and thus can be outside of the ensemble average operation. When $X(f)$ is white noise, the cross-spectral term between $N(f)$ and $X(f)$ asymptotically vanishes with increasing the number of

ensemble average. Therefore, we can estimate the system transfer function even in the presence of significant noise using the following equation

$$H(f) = \frac{E[Y(f)X(f)^*]}{E[X(f)X(f)^*]} = \frac{S_{YX}(f)}{S_{XX}(f)} \qquad (A4)$$

where $S_{YX}(f)$ is the cross-spectral density function between input and output, and $S_{XX}(f)$ is the autospectral (also called power spectral) density function of the input. Because $H(f)$ is a quotient, it is important to make $S_{XX}(f)$ sufficiently large for accurate determination of $H(f)$ over the frequency range of interest. The white noise input, which is rich in frequency components, is the most appropriate for $H(f)$ determination.

White-noise analysis vs. other system identification methods. Theoretically, $h(t)$ corresponds to the system response obtained by an impulse input. The system step response, derived from the time integral of $h(t)$, can be measured from the system response to a step input. However, the system identification method using the impulse or step input based on a single experimental trial is susceptible to unintentional noise in the output signal commonly encountered in the physiological experiments. To reduce the noise effects, repeated measurements of the system response to an identical stimulus should be averaged. In addition, an exact impulse or step input is unrealizable in many circumstances. To correct the deviation of the actual input from the ideal input, the measured system response should be deconvolved by the actual input signal, making the system identification procedure more complex than the ideal case. Taken together, measuring the system response to the impulse or step input may not necessarily be better or easier than the white noise analysis in terms of the required experimental duration and the computational burden when considering actual applications.

Other system identification methods frequently used are time-domain parametric estimation approaches such as an autoregressive moving average model. The parametric system identification methods are dependent on the model specification. If the order of the model is much greater than that of a system under study, the model becomes susceptible to subtle noises in measurements that are not actual system response. If the order of the model is much less than that of a system, the model lacks the freedom for accurate system description. The sampling interval also has a great influence on the system identification result (1). Therefore, the model order and sampling interval for the time-domain parametric estimation should be specified based on some knowledge of the system being analyzed. In contrast, the nonparametric frequency-domain analysis employed in the present study does not impose any assumptions on the system characteristics except for the linearity. Therefore, the white-noise analysis may be most suitable for exploring changes in system characteristics.

GRANTS

REFERENCES

1. Åström KJ. On the choice of sampling rates in parametric identification of time series. *Inform Sciences* 1: 279–295, 1969.
2. Åström KJ and Hägglund T. *PID Controllers: Theory, Design, and Tuning* (2nd ed). Research Triangle Park, NC: Instrument Society of America, 1995.
3. Bendat J and Piersol A. *Random Data Analysis and Measurement Procedures* (3rd ed). New York: Wiley, 2000, p.189–271.
4. Berger RD, Saul JP, and Cohen RJ. Transfer function analysis of autonomic regulation. I. Canine atrial rate response. *Am J Physiol Heart Circ Physiol* 256: H142–H152, 1989.
5. Bertram D, Barrès C, Cheng Y, and Julien C. Norepinephrine reuptake, baroreflex dynamics, and arterial pressure variability in rats. *Am J Physiol Regul Integr Comp Physiol* 279: R1257–R1267, 2000.
6. Brigham EO. FFT transform applications. In: *The Fast Fourier Transform and Its Applications*. Englewood Cliff, NJ: Prentice-Hall, 1988, p. 167–203.
7. Carson RP, Diedrich A, and Robertson D. Autonomic control after blockade of the norepinephrine transporter: a model of orthostatic intolerance. *J Appl Physiol* 93: 2192–2198, 2002.
8. Cohen MD, Finberg J, Dibner-Dunlap M, Yuih SN, and Thames MD. Effects of desipramine hydrochloride on peripheral sympathetic nerve activity. *Am J Physiol Regul Integr Comp Physiol* 258: R876–R882, 1990.
9. DiBona GF and Sawin LL. Functional significance of the pattern of renal sympathetic nerve activation. *Am J Physiol Regul Integr Comp Physiol* 277: R346–R353, 1999.
10. Dilsaver SC and Davidson R. Cholinergic properties of desipramine and amoxapine: assessment using a thermoregulation paradigm. *Prog Neuropsychopharmacol Biol Psychiatry* 11: 581–599, 1987.
11. Dorward PK, Saigusa T, and Eisenhofer G. Differential effects of central and peripheral desipramine on sympathoadrenal function and heart rate in conscious rabbits. *J Cardiovasc Pharmacol* 17: 519–531, 1991.
12. Eisenhofer G, Saigusa T, Esler MD, Cox HS, Angus JA, and Dorward PK. Central sympathoinhibition and peripheral neuronal uptake blockade after desipramine in rabbits. *Am J Physiol Regul Integr Comp Physiol* 260: R824–R832, 1991.
13. Felder RB, Heesch CM, and Thames MD. Reflex modulation of carotid sinus baroreceptor activity in the dog. *Am J Physiol Heart Circ Physiol* 244: H437–H443, 1983.
14. Glantz SA. *Primer of Biostatistics* (5th ed). New York: McGraw-Hill, 2002.
15. Goldstein DS, Brush JE Jr, Eisenhofer G, Stull R, and Esler M. In vivo measurement of neuronal uptake of norepinephrine in the human heart. *Circulation* 78: 41–48, 1988.
16. Ikeda Y, Kawada T, Sugimachi M, Kawaguchi O, Shishido T, Sato T, Miyano H, Matsuura W, Alexander J Jr, and Sunagawa K. Neural arc of baroreflex optimizes dynamic pressure regulation in achieving both stability and quickness. *Am J Physiol Heart Circ Physiol* 271: H882–H890, 1996.
17. Kashihara K, Kawada T, Yanagiya Y, Uemura K, Inagaki M, Takaki H, Sugimachi M, and Sunagawa K. The Bezold-Jarisch reflex attenuates dynamic gain of the baroreflex neural arc. *Am J Physiol Heart Circ Physiol* 285: H833–H840, 2003.
18. Kawada T, Ikeda Y, Sugimachi M, Shishido T, Kawaguchi O, Yamazaki T, Alexander J Jr, and Sunagawa K. Bidirectional augmentation of heart rate regulation by autonomic nervous system in rabbits. *Am J Physiol Heart Circ Physiol* 271: H288–H295, 1996.
19. Kawada T, Shishido T, Inagaki M, Tatewaki T, Zheng C, Yanagiya Y, Sugimachi M, and Sunagawa K. Differential dynamic baroreflex regulation of cardiac and renal sympathetic nerve activities. *Am J Physiol Heart Circ Physiol* 280: H1581–H1590, 2001.
20. Kawada T, Uemura K, Kashihara K, Jin Y, Li M, Zheng C, Sugimachi M, and Sunagawa K. Uniformity in dynamic baroreflex regulation of left and right cardiac sympathetic nerve activities. *Am J Physiol Regul Integr Comp Physiol* 284: R1506–R1512, 2003.
21. Kawada T, Yanagiya Y, Uemura K, Miyamoto T, Zheng C, Li M, Sugimachi M, and Sunagawa K. Input-size dependence of the baroreflex neural arc transfer characteristics. *Am J Physiol Heart Circ Physiol* 284: H404–H415, 2003.
22. Kawada T, Zheng C, Yanagiya Y, Uemura K, Miyamoto T, Inagaki M, Shishido T, Sugimachi M, and Sunagawa K. High-cut characteristics of the baroreflex neural arc preserve baroreflex gain against pulsatile pressure. *Am J Physiol Heart Circ Physiol* 282: H1149–H1156, 2002.
23. Levy MN. Sympathetic-parasympathetic interactions in the heart. *Circ Res* 29: 437–445, 1971.
24. Liu H, Guild S, Ringwood J, Barrett CJ, Leonard BL, Nguang S, Navakatikyan MA, and Malpas SC. Dynamic baroreflex control of blood pressure: influence of the heart vs. peripheral resistance. *Am J Physiol Regul Integr Comp Physiol* 283: R533–R542, 2002.
25. Marmarelis PZ and Marmarelis VZ. The white noise method in system identification. In: *Analysis of Physiological Systems*. New York: Plenum, 1978, p. 131–221.
26. Nakahara T, Kawada T, Sugimachi M, Miyano H, Sato T, Shishido T, Yoshimura R, Miyashita H, Inagaki M, Alexander J Jr, and Sunagawa K. Neuronal uptake affects dynamic characteristics of heart rate

response to sympathetic stimulation. *Am J Physiol Regul Integr Comp Physiol* 277: R140–R146, 1999.

27. Nicholls DG. *Proteins, Transmitters and Synapses*. Oxford, UK: Blackwell Science, 1994, p. 200–221.

28. Novi AM. An electron microscopic study of the innervation of papillary muscles in the rat. *Anat Rec* 160: 123–141, 1968.

29. Papoulis A and Pillai SU. *Probability, Random Variables and Stochastic Processes* (4th ed). Boston, MA: McGraw-Hill, p. 435–498.

30. Rumantir MS, Kaye DM, Jennings GL, Vaz M, Hastings JA, and Esler MD. Phenotypic evidence of faulty neuronal norepinephrine reuptake in essential hypertension. *Hypertension* 36: 824–829, 2000.

31. Saper CB. Brain stem modulation of sensation, movement, and consciousness. In: *Principles of Neural Science* (4th ed), edited by Kandel ER, Schwartz JH, and Jessell TM. New York: McGraw-Hill, 2000, p. 889–909.

32. Schroeder C, Tank J, Boschmann M, Diedrich A, Sharma AM, Biaggioni I, Luft FC, and Jordan J. Selective norepinephrine reuptake

inhibition as a human model of orthostatic intolerance. *Circulation* 105: 347–353, 2002.

33. Shannon JR, Flattem NL, Jordan J, Jacob G, Black BK, Biaggioni I, Blakely RD, and Robertson D. Orthostatic intolerance and tachycardia associated with norepinephrine-transporter deficiency. *N Engl J Med* 342: 541–549, 2000.

34. Sugimachi M, Imaizumi T, Sunagawa K, Hirooka Y, Todaka K, Takeshita A, and Nakamura M. A new method to identify dynamic transduction properties of aortic baroreceptors. *Am J Physiol Heart Circ Physiol* 258: H887–H895, 1990.

35. Suzuki S, Ando S, Imaizumi T, and Takeshita A. Effects of anesthesia on sympathetic nerve rhythm: power spectral analysis. *J Auton Nerv Syst* 43: 51–58, 1993.

36. Tank J, Schroeder C, Diedrich A, Szczech E, Haertter S, Sharma AM, Luft FC, and Jordan J. Selective impairment in sympathetic vasomotor control with norepinephrine transporter inhibition. *Circulation* 107: 2949–2954, 2003.

A novel framework of circulatory equilibrium

Kazunori Uemura,[1] Masaru Sugimachi,[1] Toru Kawada,[1] Atsunori Kamiya,[1]
Yintie Jin,[1,2] Koji Kashihara,[1,2] and Kenji Sunagawa[1]

[1]Department of Cardiovascular Dynamics, National Cardiovascular Center Research Institute,
Suita 565-8565; and [2]Organization for Pharmaceutical Safety and Research, Tokyo 100-0013, Japan

Uemura, Kazunori, Masaru Sugimachi, Toru Kawada, At-sunori Kamiya, Yintie Jin, Koji Kashihara, and Kenji Sunagawa. A novel framework of circulatory equilibrium. Am J Physiol Heart Circ Physiol 286: H2376–H2385, 2004. First published February 5, 2004; 10.1152/ajpheart.00654.2003.—A novel framework of circulatory equilibrium was developed by extending Guyton's original concept. In this framework, venous return (CO_V) for a given stressed volume (V) was characterized by a flat surface as a function of right atrial pressure (P_{RA}) and left atrial pressure (P_{LA}) as follows: $CO_V = V/W - G_SP_{RA} - G_PP_{LA}$, where W, G_S, and G_P denote linear parameters. In seven dogs under total heart bypass, CO_V, P_{RA}, P_{LA}, and V were varied to determine the three parameters in each animal with use of multivariate analysis. The coefficient of determination ($r^2 = 0.92$–0.99) indicated the flatness of the venous return surface. The averaged surface was $CO_V = V/0.129 - 19.61P_{RA} - 3.49P_{LA}$. To examine the invariability of the surface parameters among animals, we predicted the circulatory equilibrium in response to changes in stressed volume in another 12 dogs under normal and heart failure conditions. This was achieved by equating the standard surface with the individually measured cardiac output (CO) curve. In this way, we could predict CO [$y = 0.90x + 5.6$, $r^2 = 0.95$, standard error of the estimate (SEE) = 8.7 ml·min^{-1}·kg^{-1}], P_{RA} ($y = 0.96x$, $r^2 = 0.98$, SEE = 0.2 mmHg), and P_{LA} ($y = 0.89x + 0.5$, $r^2 = 0.98$, SEE = 0.8 mmHg) reasonably well. We conclude that the venous return surface accurately represents the venous return properties of the systemic and pulmonary circulations. The characteristics of the venous return surface are invariable enough among animals, making it possible to predict circulatory equilibrium, even if those characteristics are unknown in individual animals.

venous return; cardiac output; hemodynamics

THE FRAMEWORK FOR CIRCULATORY EQUILIBRIUM was pioneered by Guyton and associates in the 1950s (14–17). They characterized the venous return properties of the systemic vein by the venous return curve and the apparent pumping ability of the cardiothoracic compartment by the cardiac output (CO) curve (Fig. 1A). The intersection of the two curves determines equilibrium CO and right atrial pressure (P_{RA}) (14). This concept clearly defined the circulatory equilibrium under rather simple pathophysiological conditions, such as hemorrhage and exercise, and deepened our understanding of control mechanisms of CO. However, because the original framework lumped various subsystem components, such as the right ventricle, pulmonary vascular system, and left ventricle, into a single cardiothoracic compartment, the lack of consideration of the venous return properties of the pulmonary circulation and the pumping ability of the individual ventricles makes it difficult to define the circulatory equilibrium under more complex condi-

tions such as unilateral ventricular failures, which are often seen in clinical settings (2). In other words, redistribution of blood between the systemic and pulmonary circulations cannot be defined by their original framework.

To deal with the blood redistribution, Guyton et al. (15) modified the original framework and developed a two-compartment model. However, the analysis of hemodynamics by this two-compartment model is rather complex. In this model, left ventricular CO is determined as the equilibrium between left ventricular CO and pulmonary venous return. Similarly, right ventricular CO is determined as the equilibrium between right ventricular CO and systemic venous return. They derived equilibrium CO of the total circulation by iteratively redistributing stressed blood volume between the two compartments until the CO of the two compartments matched (15). The complexity of the analysis makes application to hemodynamic analysis impractical in the clinical setting.

To overcome the limitation of the framework of Guyton et al., Sunagawa et al. (24, 30) proposed a novel framework of circulatory equilibrium. In the framework of Sunagawa et al., the venous return properties of the systemic and pulmonary circulations are integrated to deal with blood volume redistribution between the two circulations. A mathematical analysis using a simple linearized model (see APPENDIX) indicated that venous return (CO_V) for a given stressed volume (V) forms a flat surface (venous return surface) as a function of P_{RA} and left atrial pressure (P_{LA}; Fig. 1B). This is formulated as follows

$$CO_v = V/W - G_SP_{RA} - G_PP_{LA} \qquad (1)$$

where W denotes the parameter that defines the maximum venous return for the given stressed volume and G_S and G_P are slopes of venous return with respect to P_{RA} and P_{LA}, respectively. As we show in the APPENDIX, these three linear parameters reflect vascular compliance and resistance. The circulatory equilibrium is given as the intersection of the venous return surface and the integrated CO curve, defined as a function of P_{RA} and P_{LA}, thereby representing bilateral ventricular function (24, 30). Changes in V shift the venous return surface upward and downward, thereby altering the equilibrium point accordingly.

This extended framework of Guyton et al. allows us to predict circulatory equilibrium, even in the presence of unilateral ventricular dysfunction, making it useful in clinical settings where complex pathophysiologies must be interpreted. With this framework for guidance, proper management of low CO and/or pulmonary congestion should improve the prognosis of cardiac patients (10, 21). However, the characteristics of
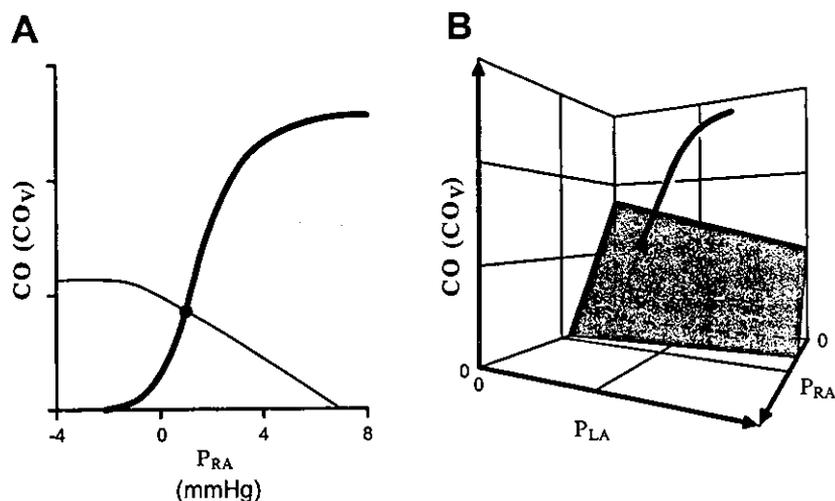
A

B

Fig. 1. A: equilibrium diagram, based on the theory of Guyton et al. (14–17), to illustrate the relation between right atrial pressure (P_{RA}), venous return (CO_V), and cardiac output (CO). Equilibrium CO and P_{RA} are obtained as the intersection of the CO curve (thick curve) and the venous return curve (thin curve). B: equilibrium diagram, based on the theory of Sunagawa et al. (30), to illustrate the relation between P_{RA}, left atrial pressure (P_{LA}), CO_V, and CO. Equilibrium CO, P_{RA}, and P_{LA} are obtained as the intersection of venous return surface (shaded area) and integrated CO curve (thick curve). When total stressed blood volume is increased, the surface shifts upward, as does the new equilibrium point (not shown).

the venous return surface have never been experimentally studied. Therefore, it is not known whether the simple flat surface represents the integrated venous return of the pulmonary and systemic circulations.

The purpose of this investigation was to experimentally validate the concept of the venous return surface (24, 30). To examine the characteristics of the venous return surface, we determined W, G_S, and G_P using a total heart bypass preparation. To examine the invariability of the characteristics of the venous return surface under a range of stressed volumes among animals, we predicted the circulatory equilibrium from the intersection of the measured integrated CO curve and the venous return surface, as defined by the standard set of parameters. The results indicated that the venous return surface was indeed remarkably flat. Its parameter values were invariable enough among animals that circulatory equilibrium for a given integrated CO curve could be predicted under unilateral heart failure as well as during normal cardiac function.

METHODS

Preparation

Care of the animals was in strict accordance with the guiding principles of the Physiological Society of Japan. We used seven adult male mongrel dogs (26.3 ± 2.4 kg) for examination of the venous return surface and another 12 male dogs (26.1 ± 3.2 kg) for measurement of the integrated CO curve to predict circulatory equilibrium.

Dogs were anesthetized with pentobarbital sodium (25 mg/kg) and intubated endotracheally. Urethane (250 mg/ml) and α-chloralose (40 mg/ml) were continuously infused (0.3 ml$\cdot$kg$^{-1}\cdot$h^{-1}) to maintain an appropriate level of anesthesia during the experiments. A 5F catheter was placed in the right femoral vein for administration and withdrawal of blood, fluids, and drugs. To stabilize autonomic tone, we isolated the carotid sinus bilaterally and kept the intrasinus pressure constant (120 mmHg) (27). The cervical vagosympathetic trunks were cut to eliminate their buffering effects. Systemic arterial pressure was measured through a fluid-filled catheter placed in the thoracic aorta via the left common carotid artery and connected to a pressure transducer (model DX-200, Nihon Kohden). After a median sternotomy, the heart was suspended in a pericardial cradle. Fluid-filled catheters were placed in the right and left atrium and in the main trunk of the pulmonary artery for measurement of P_{RA}, P_{LA}, and pulmonary arterial pressure, respectively. The junction of the vena cava and the right atrium was taken as the reference point for zero pressure.

To examine the venous return surface, we performed a total heart bypass (Fig. 2). The perfusion system was initially primed with ~200 ml of heparinized blood from another dog. Two roller pumps (MERA) were used to control systemic and pulmonary flows. A systemic perfusion cannula was placed in the right common carotid artery. A draining cannula for the systemic circulation was inserted into the right ventricle through its free wall. A pulmonary perfusion cannula was placed in the pulmonary artery through the right ventricle. A draining cannula for the pulmonary circulation was introduced into the left ventricle via the apex. The flow rates of both pumps were measured by in-line electromagnetic flow probes (model MFV-2100, Nihon Kohden). The two probes were simultaneously calibrated using a graduated cylinder. Both pumps began with an initial flow rate of 80 ml$\cdot$min$^{-1}\cdot$kg^{-1}. Finally, umbilical tape placed around the pulmonary artery to hold the pulmonary cannula was tightened, and the ascending aorta was clamped, thus switching to the total heart bypass. Ligation of the coronary arteries arrested the heart.

For measurement of the integrated CO curve, we maintained circulation by the native hearts, not by the mechanical pumps. The surgical procedures were the same as those used for examination of the venous return surface up to placement of the pressure catheters. CO was measured by an ultrasound flow probe placed around the ascending aorta (Transonics, Ithaca, NY).
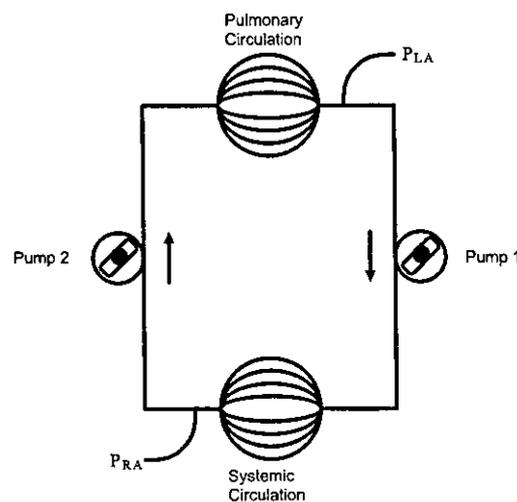

Fig. 2. Schematic representation of experimental setup used to characterize the venous return surface. Systemic and pulmonary circulations are perfused by pumps *1* and *2*, respectively. Venous outflow is drawn directly into the pumps without passing through a reservoir.
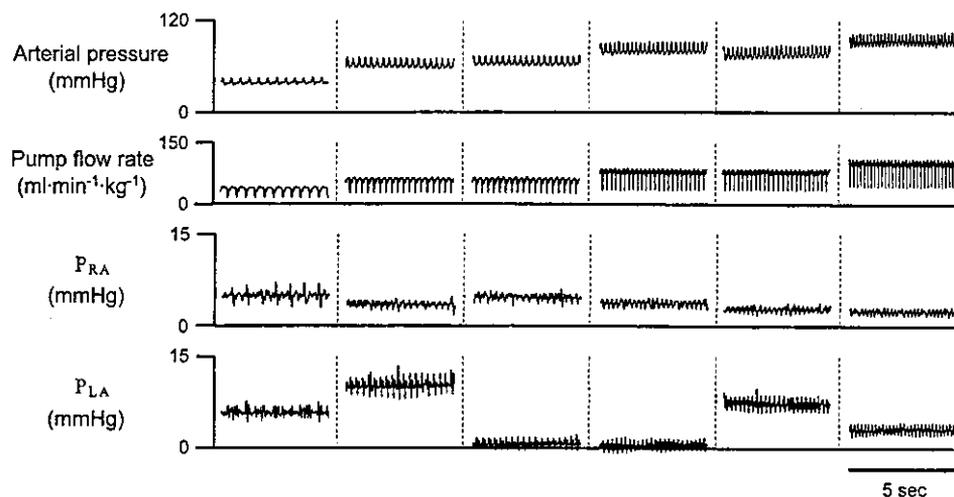
Fig. 3. A set of 6 recordings of arterial pressure, pump flow rate, P_RA, and P_LA. Only those traces that reached steady state are shown. Transient unbalancing of flow rates of *pumps 1* and *2* induced blood redistribution between systemic and pulmonary circulations. P_RA and P_LA were changed over as wide a range as possible. Pump flow rates were increased stepwise.

Experimental Protocol

Characterization of the venous return surface. After a stable condition was obtained, the flow rates of both pumps were varied stepwise from 40 to 100 $ml \cdot min^{-1} \cdot kg^{-1}$ in 20 $ml \cdot min^{-1} \cdot kg^{-1}$ increments (Fig. 3). At flow rates of 60 and 80 $ml \cdot min^{-1} \cdot kg^{-1}$, we varied the blood volume distribution between the pulmonary and systemic circuits by transiently unbalancing the flow rates of the two pumps. Steady state was attained in each flow rate within 50 s. In each step, we measured pump flow rate and bilateral atrial pressure during temporary suspension of ventilation at end expiration. We obtained a total of six recordings in each dog. To estimate W, we removed or added blood volume by -5 to $+4$ ml/kg, which was assumed to alter only the stressed blood volume. Because we isolated the baroreceptors, baroreflex-related changes in unstressed volume were negligible. We then repeated the same protocol.

Measurement of the integrated CO curve for prediction of circulatory equilibrium. In six dogs, to alter CO over a wide range, we first infused ~200 ml of whole blood. We then withdrew blood in 2 ml/kg steps up to a total of 10–22 ml/kg (5–11 steps for a single animal) while measuring CO and bilateral atrial pressures (Fig. 4). As in the first protocol, we assumed that this volume reduction altered only the stressed blood volume of the systemic and pulmonary circulation. We defined the reference stressed volume when half of the infused blood

was withdrawn. This reference was used when stressed volume was changed to predict circulatory equilibrium. In six other dogs, left ventricular failure was induced by embolization of the left circumflex coronary artery with glass microspheres (90 μm diameter) (35). We adjusted the number of microspheres to increase P_LA by 20 mmHg. We then volume loaded the animals and repeated the same protocol.

Data Analysis

All analog signals were digitized at 200 Hz with a 12-bit analog-to-digital converter (Contec, Osaka, Japan) using a dedicated laboratory computer system; the data were then stored on a hard disk for subsequent analysis. All the recorded data were averaged over 5 s and expressed as means $\pm$ SD. All data, excluding pressure data, were normalized to individual body weight. The level of statistical significance was defined as $P < 0.05$.

Derivation of parameters of the venous return surface. We used the algebraic mean of the flow rates of *pumps 1* and *2* as CO_V. A multivariate linear regression was performed on a set of six recordings, with *Eq. 1* used to derive G_S and G_P in each dog. We repeated the same analysis when the stressed volume was changed. Because changes in the stressed volume did not significantly affect G_S or G_P, we derived W as the ratio of changes in stressed volume to the amount of parallel shift of the venous return surface (see APPENDIX). To test the
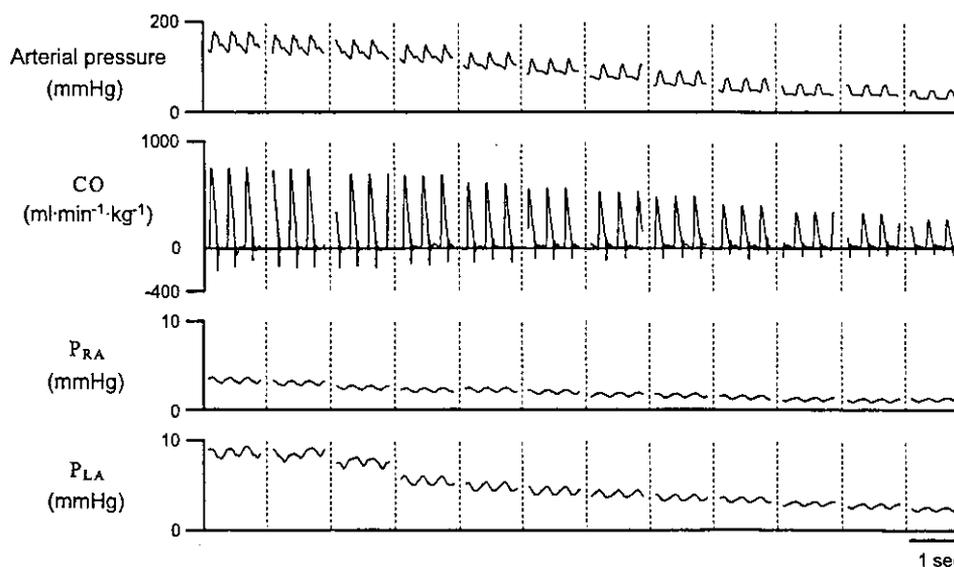

Fig. 4. Changes in arterial pressure, CO, P_RA, and P_LA during the study to measure the integrated CO curve. As P_RA and P_LA decreased after stepwise reductions of stressed blood volume, CO also decreased (Frank-Starling mechanism).

goodness of fit of the multivariate regression equation as a representation of the venous return surface, the multiple coefficient of determination (r^2) and the standard error of estimate (SEE) were calculated. To estimate the error relative to the average value of the respective parameters, we derived coefficients of variation for G_S, G_P, and W.

Prediction of Circulatory Equilibrium

To characterize the CO curve for each animal as a function of P_{RA} and P_{LA}, we fitted CO as a function of P_{RA} using a three-parameter logarithmic curve

$$CO = \alpha_R \ln (P_{RA} - \beta_R) + \gamma_R \quad (2)$$

and CO as a function of P_{LA} using

$$CO = \alpha_L \ln (P_{LA} - \beta_L) + \gamma_L \quad (3)$$

Coefficients of fitted logarithmic functions, α_R, β_R, and γ_R and α_L, β_L, and γ_L, characterized the CO curve of the right and left heart, respectively. They were determined by the least-squares method (Fig. 5A).

To predict the equilibrium points for each animal, we used the standard set of parameters of the venous return surface derived from the first protocol to determine the venous return surface for a given change in stressed volume. We then numerically estimated the intersection of the venous return surface and the integrated CO curve given by Eqs. 2 and 3 (Fig. 5B). This was achieved by simultaneously solving Eqs. 1–3 for CO, P_{LA}, and P_{RA}. The predicted CO, P_{RA}, and P_{LA} were compared with measured CO, P_{RA}, and P_{LA}.

RESULTS

Venous Return Surface

Figure 6 shows a representative venous return surface as a function of P_{RA} and P_{LA}. All six points measured are aligned on a unique flat surface. The alignment is even clearer if the data points are viewed from a direction parallel to the surface (Fig. 6, inset). The six points obtained from each animal were closely aligned on a flat surface (Fig. 7). Table 1 summarizes the parameter values obtained from seven dogs. The fact that the multiple correlation of determination was close to unity ($r^2 = 0.92$–0.99), with a small SEE relative to the amount of venous return, suggested that the approximation of venous return by a flat surface was reasonably accurate.

Parameter values defining the venous return surface did not differ markedly among animals. Coefficients of variation of W, G_S, and G_P were 38, 11, and 17%, respectively. From these data, we defined the standard venous return surface as follows:
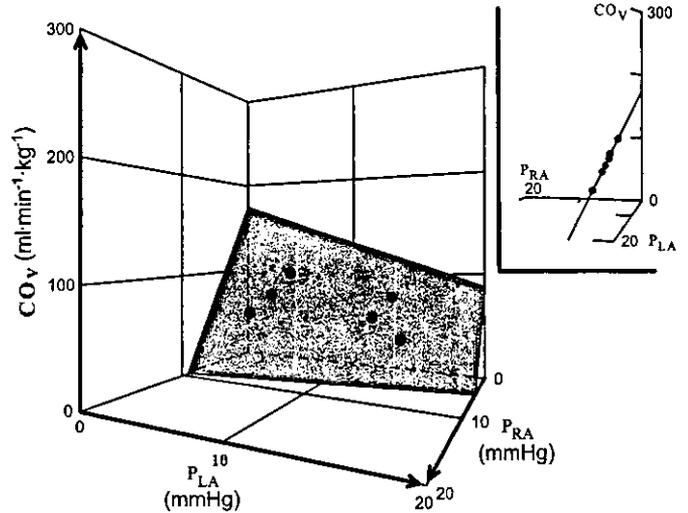

Fig. 6. Venous return (CO_V) plotted against simultaneously obtained P_{RA} and P_{LA} in a representative case. A venous return surface determined by a set of 6 recordings is superimposed. Inset: 6 points and surface are viewed from a direction parallel to the surface. The 6 points are aligned closely along a single line and lie on a single surface, i.e., venous return surface.

$CO_V = V/0.129 - 19.61P_{RA} - 3.49P_{LA}$. With different animals, this standard venous return surface was used to predict circulatory equilibrium under a variety of stressed volumes and cardiac functions in the second protocol.

Prediction of CO, P_{RA}, and P_{LA}

Table 2 shows a summary of the approximation of the integrated CO using a three-parameter logarithmic curve. In each animal, the coefficient of determination was high for the CO curve of the right ventricle ($r^2 = 0.96$–0.99) and the left ventricle ($r^2 = 0.89$–0.99) under normal cardiac conditions. In other words, the logarithmic curves represented the integrated CO curve with reasonable accuracy. The logarithmic function remained a good approximation under the condition of unilateral heart failure, as evidenced by the high coefficients of determination: $r^2 = 0.73$–0.99 and 0.84–0.99 for the CO curves of the right and left ventricles, respectively.

Using the standard venous return surface, we predicted circulatory equilibrium by determining the intersection of the venous return surface and the integrated CO curve under a variety of stressed volumes and cardiac functions. Figure 8A
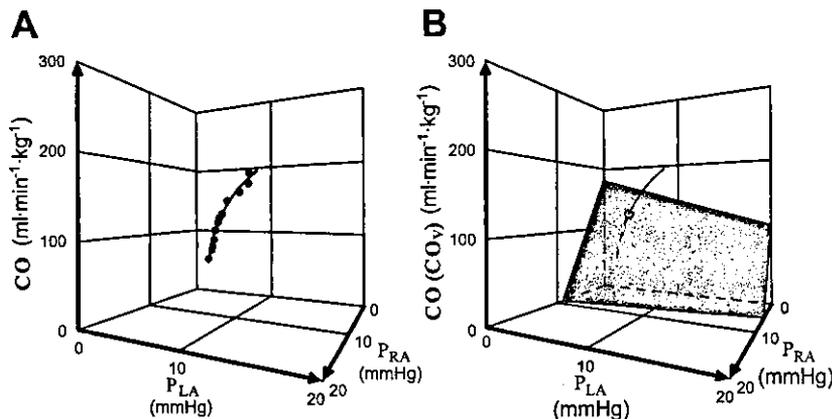

Fig. 5. A: CO of a dog plotted against simultaneously obtained P_{RA} and P_{LA}. Solid line, satisfying Eqs. 2 and 3, represents the integrated CO curve. B: intersection (o) of the standard venous return surface and the integrated CO curve gives the predicted CO, P_{RA}, and P_{LA}.
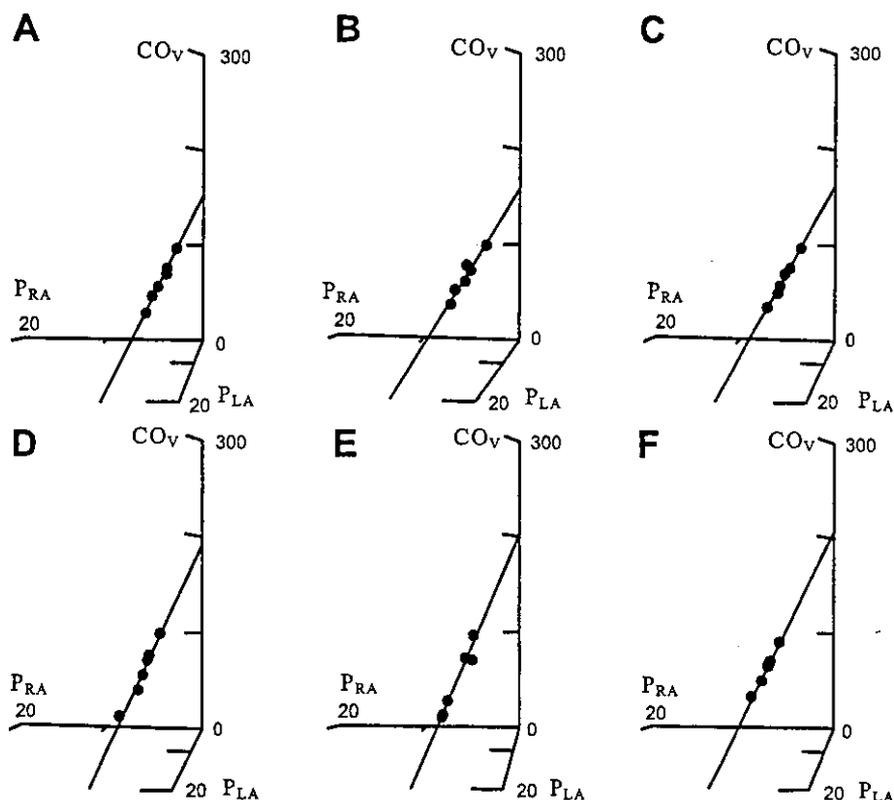
Fig. 7. Venous return surfaces from 6 dogs. In *A–F*, the 6 points are closely aligned on their own surfaces. CO_V is expressed in $ml \cdot min^{-1} \cdot kg^{-1}$ and P_{RA} and P_{LA} in mmHg.

shows the relations between predicted and measured CO. CO was predicted with reasonable accuracy ($y = 0.90x + 5.6$, $n = 104$, $r^2 = 0.95$, SEE $= 8.7$ $ml \cdot min^{-1} \cdot kg^{-1}$), despite large changes in CO: from 40 to 220 $ml \cdot min^{-1} \cdot kg^{-1}$. The ratio of SEE to the mean of the predicted CO was 0.090, indicating small variability around the regression line. A small intercept value with near unity slope also indicates the accuracy of prediction. Thus it is fair to say that this framework predicted CO reasonably well, irrespective of cardiac conditions, i.e., normal or left heart failure.

P_{RA} was also predicted accurately, regardless of stressed volume and cardiac function ($y = 0.96x$, $n = 104$, $r^2 = 0.98$, SEE $= 0.2$ mmHg; Fig. 8*B*). The ratio of SEE to the mean of the predicted P_{RA} was 0.069. From as low as 1 mmHg to as high as 8 mmHg, P_{RA} could be predicted accurately.

Predicted P_{LA}, as a whole, agreed reasonably well with P_{LA} measured over a wide range ($y = 0.89x + 0.5$, $n = 104$, $r^2 = 0.98$, SEE $= 0.8$ mmHg; Fig. 8*C*). The ratio of SEE to the mean of the predicted P_{LA} was 0.087.

DISCUSSION

We have shown that a linear model of venous return, i.e., the venous return surface, characterizes the venous return properties of the systemic and pulmonary circulations with reasonable accuracy. The surface was, in fact, remarkably flat. When the venous return surface, with standard parameters, was equated with the integrated CO curves of different animals under a variety of stressed volumes and cardiac functions, the predicted CO, P_{RA}, and P_{LA} agreed well with measured values. These results strongly support the validity of the venous return surface concept (24, 30) and suggest its usefulness in the clinical setting.

Characteristics of the Venous Return Surface

The venous return surface was remarkably flat. Its flatness is attributable to the constant nature of W, G_S, and G_P during changes in loading conditions. Because these parameters are a complex function of vascular resistance and compliance and

Table 1. *Parameter values characterizing the venous return surface*

Dog No.	G_S	G_P	W	r^2	SEE
1	19.77	3.83	0.154	0.99	1.9
2	23.30	3.39	0.232	0.92	7.4
3	20.99	4.04	0.099	0.97	3.7
4	17.60	2.92	0.088	0.99	1.3
5	16.17	3.46	0.092	0.92	6.5
6	19.01	4.26	0.107	0.99	1.5
7	20.44	2.55	0.132	0.99	1.2
Mean±SD	19.61 ± 2.33	3.49 ± 0.61	0.129 ± 0.051	0.97	3.4 ± 2.6

G_S ($ml \cdot min^{-1} \cdot mmHg^{-1} \cdot kg^{-1}$), G_P ($ml \cdot min^{-1} \cdot mmHg^{-1} \cdot kg^{-1}$), and W (min) are parameters characterizing venous return surface. See METHODS for calculations. r^2, coefficient of determination; SEE, standard error of the estimate ($ml \cdot min^{-1} \cdot kg^{-1}$).